Physics Institute, Pontificia Universidad Católica de Chile

Medicine Faculty, Heidelberg University

Measurement of energy deposition of therapeutic ion beams using a 100 µm thick pixelated semiconductor detector Timepix

Karen Romero Sánchez

A thesis submitted in the fulfillment of the requirements for the degree of *Master in Clinical Medical Physics*

Supervisor: Dr. Mária Martišíková

Co-supervisor: Dr. Paola Caprile

September 2018

Measurement of energy deposition of therapeutic ion beams using a 100 µm thick pixelated semiconductor detector Timepix

ABSTRACT

Recently there has been an increasing interest in the implementation of different sources of radiation to treat challenging situations which include deep seated radioresistant tumors and pediatric patients. In this regard ion beam radiotherapy plays an important role, thanks to its characteristic confined dose deposition and low entrance and exit doses. For the prediction of its radiobiological effect, it becomes necessary to verify the energy deposition of single ions accurately. However, measuring devices for a realistic clinical application for a position-resolved assessment of the distributions are widely lacking.

In this work, the capabilities of a Timepix pixelated semiconductor detector with a 100 µm thick silicon sensor to measure single-ion energy depositions were investigated. Energy loss spectra were analyzed with respect to the mean deposited energy and the width of the distributions. The results were compared to expected behaviors from Monte Carlo simulations. A good agreement between measurements and simulations was found in the range of 0.638 MeV/mm to 18.196 MeV/mm mean deposited energy in silicon, with deviations below 10%. The corresponding deviations in the width of the spectra were between 1.1% and 18.2%. However, significant differences with respect to simulations were observed in ^{12}C and ^{16}O energy loss spectra, reaching deviations up to 38.6% (mean deposited energy) and 303.6% (spectrum width).

The detector's performance was compared with that of a Timepix with a 300 µm thick sensor. Due to the reduced sensor thickness, leading to lower registered signals, the 100 µm detector measured the energy deposits in some cases more accurately. In particular, a significantly improved response to deposited energies above 2.81 MeV/mm by at least a factor of 2 was found. Below 0.89 MeV/mm the performance of the 100 µm sensor was limited by too low signals.

The results of this thesis highlight the capabilities and limitations of thin Timepix detectors in measuring energy deposition in a wide range of types and energies of therapeutic ion beams.

Declaration:

I hereby certify, that I have composed the Master's Thesis independently, that no source materials or aids other than those mentioned have been used and that all citations have been declared appropriately.

Puebla, Mexico, July, 2018 _____

Karen Romero Sánchez

Nomenclature and abbreviations

BAMS: Beam **A**pplication and **M**onitoring **S**ystem

Cluster: Set of pixels with non-zero values, adjacent to each other.

Cluster volume: The sum of the values of every pixel belonging to the same cluster.

FLUKA: FLUktuirende **KA**skade

Frame: Period of time in which Timepix acquires information.

FWHM: Full **W**idth at **H**alf **M**aximum

HIT: Heidelberg **I**on **B**eam **T**herapy **C**enter

LET: Linear **E**nergy **T**ransfer

MC: Monte **C**arlo

Ok cluster: During measurements, a cluster size criterion to have statistics of the acquired number of clusters has to be set in the *FITPIX* software. In this way, the software counts those clusters that have met the criteria in real time. With this information, the user can decide whether to continue or to stop the measurements.

Rim: Pixels with a low Time over Threshold (TOT) value in a cluster located far away from the cluster's center.

RT: Radiation **T**herapy

PS: Phase **S**pace

WHO: World **H**ealth **O**rganization

A mis bien y muy amados hermanos, mamá y habibi

To my beloved brethren, mom and habibi

CONTENT

"Somewhere, something incredible is waiting to be known."
Carl Sagan

1 Introduction

Cancer is currently a growing public health problem around the globe, representing the second leading cause of death [1]. Based on estimations by the International Agency for Research on Cancer (IARC), there were 14.1 million new cancer cases in 2012 worldwide [2]. In 2015, deaths from cancer were estimated to be as many as 8.8 million [3], and by 2030 the global burden is expected to grow to 21.7 million new cancer cases and 13 million cancer deaths [2]. There are different modalities available to treat cancer which can be implemented alone or in combination: from traditional options like surgery and chemotherapy to techniques like radiotherapy (RT) and immunotherapy. Since 2005, the proportion of patients presenting clinical attributes that suggest they could benefit from RT accounts for more than 50% [4], therefore such treatment technique plays a significant role in the combat against cancer.

As this health problem has a major impact on the well-being of the world's population, great effort is being made to provide more effective and safe treatments that can guarantee the best outcome for the patients. In this regard, the use of heavy ions has been gaining momentum in the RT field owing to the following reasons (among others):

- The advantageous (compared with photons) depth dose profile which spares organs at risk thanks to a lower entrance dose while concentrating the maximum dose deposition in the tumor.
- A rapid fall-off of the depth dose profile which spares distal organs at risk thanks to the very low exit dose.
- The enhanced relative biological effectiveness (RBE), helpful when treating radioresistant cancer types.

Ever since heavy ions have started being adopted in clinical practice, as the increasing amount of facilities offering this radiation type demonstrates, new challenges have arisen. Examples of such challenges include reducing the uncertainties related to the range of the utilized charged particles, the standardization of clinical RBE [5] and the need of detectors to measure deposited energy with high accuracy and reproducibility. In this vein, a novel detector called Timepix has gained attention because it has shown potential applications in X-Ray fluorescence radiography, time-of-flight spectroscopy, detection of ultra-cold neutrons, neutron transmission radiography and radiography with heavy charged-particles [6]. Given the good results obtained with photon and neutron fields, it is of interest to assess the capabilities of the sensor in therapeutic ion beams. Some features like the small size, high spatial resolution and the offered operation modes (counting mode, time of arrival, energy mode) make Timepix an attractive device to be used in ion beam RT.

The aim of this work is to evaluate the energy operation mode (TOT) of the Timepix detector in order to perform energy deposition measurements in its silicon-pixelated sensitive layer. For this purpose, ^{1}H, ^{4}He, ^{12}C and ^{16}O ion beams were used as radiation source. Four[‡] different primary beam energies per ion type were analyzed. The measured deposited energy spectra were compared with Monte Carlo simulations using the FLUKA code. Two different approaches to simulate the ion beams were used, namely the “phase space” and the “BAMS” methods. A study of the mean deposited energy and the width of the deposited energy spectra was carried out.

With regard to the structure of the thesis, Chapter 2 gives a close look into the basic physic interactions of charged particles with matter and the principle of detection in silicon. In Chapter 3, the material and methods employed during the realization of this investigation are presented and described. Chapter 4 shows the main experimental and simulated Results which are explained in the following chapter, discussion and outlook. Finally, Chapter 6 presents the conclusion of this work.

[‡] Exceptionally only three primary beam energies were used with ^{12}C ions.

"A hundred times a day I remind myself that my inner and outer life depend on the labors of other men, living and dead, and that I must exert myself in order to give in the measure as I have received and am still receiving".
Albert Einstein

2

Physical Background

The physics of the phenomena involved in the measurements of this investigation is addressed in the present chapter, which is divided in two main parts: Section 2.1 covers the interactions of heavy ions with matter and Section 2.2 gives and insight in the principle of operation of silicon detectors.

2.1 Interactions of heavy ions with matter

Energetic ions can interact with electrons and the nuclei of the material they are traversing depositing an extremely high localized density of energy [7]. During their passage through matter, ions undergo collisions with the surrounding stationary atoms while losing energy and ionizing the medium. For heavy ions with a few keV/u kinetic energy the energy loss occurs predominantly by elastic scattering whereas for energies above 1-2 MeV/u the energy loss occurs mainly by inelastic scattering processes [7].

2.1.1 Energy loss

The incident ion (or projectile) continuously loses its kinetic energy by elastic and inelastic collisions with atoms of the target material. This energy loss dE/dX has three components [7]:

$$\frac{dE}{dx} = \left(\frac{dE}{dx}\right)_{nuclear} + \left(\frac{dE}{dx}\right)_{electronic} + \left(\frac{dE}{dx}\right)_{radiation} \tag{2.1}$$

The nuclear energy loss component dominates at low energies of typically 10-100 keV/u. This is caused by scattering of the projectile given the screened nuclear potential of the target atoms (elastic collisions) [8]. When the recoil energy transferred to target

atoms is higher than the binding energy, these atoms are released and can trigger off a series of recoils as long as their kinetic energy is sufficiently big.

At high energies (typically 10-100 MeV/u) [8], the energy loss is given by the interaction of the effective charge of the ion with the target electrons through inelastic collisions producing excitation or ionization. In this process, the energy is transferred to the medium through electron-phonon interaction. Electronic collisions involve small energy loss per interaction and negligible deflection of the projectile trajectory.

From the three contributions to energy loss showed in Equation 2.1, radiative processes represent the mechanism in which less amount of energy is lost by heavy ions.

2.1.2 Linear energy transfer

The concept of "Linear Energy Transfer" (LET) is used to describe quantitatively the quality of the radiation [9] and has been widely used when discussing its biological effects [10]. It is defined as the amount of average energy dE imparted per unit track length to the *immediate vicinity* of the trajectory of a charged particle in traversing a distance dl [10]. In the previous definition, "immediate vicinity" refers to the fact that only locally imparted energy is taken into account regarding either a maximum distance from the particle track or a maximum value of discrete energy loss [11]. This term is defined as:

$$LET = L = \frac{dE}{dl} \tag{2.2}$$

and it is commonly expressed in units of keV/μm.

The energy-restricted form of LET (LΔ) is defined in the ICRU Report 85 [12] as that part of the total energy loss of a charged particle due to energy transfers up to a specified energy cut-off value Δ (in eV):

$$L_{\Delta} = \left(\frac{dE}{dl}\right)_{\Delta} \tag{2.3}$$

Some LET values are shown in Table 2.1 to give a glimpse of the magnitude of this concept for some clinically used radiation.

Radiation	LET [keV/μm]
^{60}Co	0.2
250 keV XR	2
14 MeV neutrons	75
Heavy charged particles	Between 100-2000

Table 2.1 Approximated LET values for different radiation types. Taken from [9].

LET can be seen as a way to describe how sparsely ionizing radiation is (as depicted in Figure 2.1.1). This property is related to the probability of producing double strand breaks in the DNA chain of the target cells. This sort of cell damage is more difficult to be repaired and consequently cell survival is lower. If a certain dose value is considered, low-LET radiation (e.g. photons†) causes less biological damage. Instead, high-LET radiation (e.g. heavy ions) is able to produce a greater biological impact. This is the reason why high-LET radiation is the preferred choice when treating radioresistant tumors. In Figure 2.1.2 the difference in cell survival fraction for a range of dose between low and high LET radiation is illustrated.

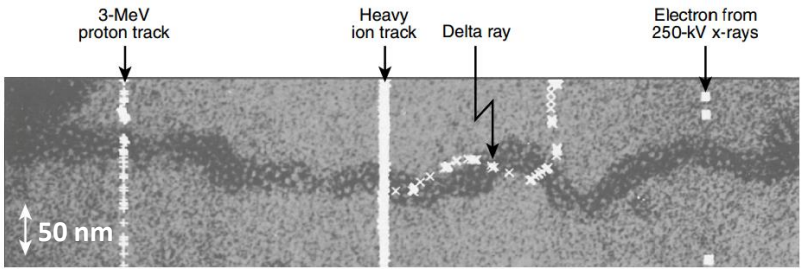

Figure 2.1.1 Computer simulations of ionization tracks in a strand of chromatin produced by different particles. Left: 3 MeV protons (medium-LET), Center: high-energy iron ion (high-LET) and Right: electron produced by 250 kVp X-Rays (low-LET). Each cross represents single ionizations. Adapted from [9].

† Even though photons are not charged particles, they produce secondary electrons that are able to ionize the medium.

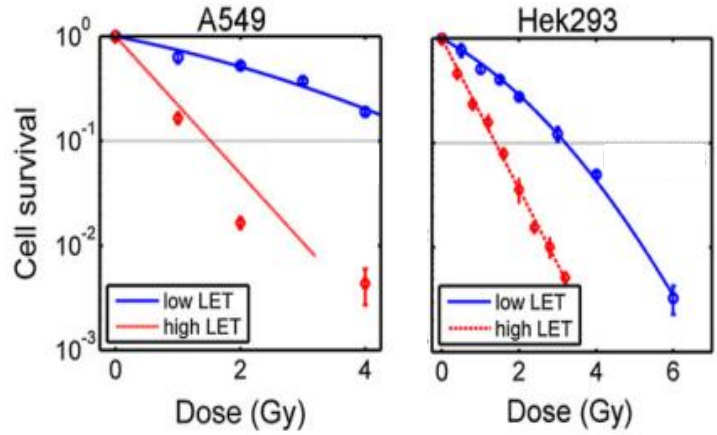

Figure 2.1.2 Two different cell lines A549 (adenocarcinomic human alveolar basal epithelial cells) and Hek293 (human embryonic kidney cells) were irradiated with low-LET (photons) and high-LET radiation (carbon ions). For a given dose, lower cell survival is observed after irradiation with carbon ions. Adapted from [13].

For heavy and low-velocity particles, the energy loss per unit track length and the LET coincide while for light and fast particles the two quantities differ considerably. This is due to the fact that part of the energy loss of an electron of several MeV is used to eject so-called δ-electrons from atoms in the medium. These δ-electrons do not contribute to the LET since they are energetic enough to make energy deposits far away from the track of the charged particle [10].

The energy loss of a high-energy charged particle in matter due to its interactions with electrons in the target material is given by the Bethe-Bloch equation:

$$\frac{dE}{dx} = \rho \frac{Z_{nucl}}{A_\rho}\left(0.307\frac{MeV cm^2}{g}\right)\frac{Z^2}{\beta^2}\left[\frac{1}{2}ln\left(\frac{2m_e c^2\beta^2\gamma^2 T_{max}}{I^2}\right) - \beta^2 - \frac{\delta(\beta)}{2}\right] \qquad (2.4)$$

Where:

dE/dx = energy loss of the projectile per unit length

Z = charge of the particle divided by the proton charge

c = velocity of light

β = v/c, with v the velocity of the projectile

$\gamma = (1-\beta^2)^{-1/2}$

ρ = density of the traversed material

Z_{nucl} = dimensionless charge of the nuclei

A_ρ = relative atomic weight

I = mean excitation energy of the traversed material in eV

T_{max} = maximum energy transfer to a free electron in a single collision

δ(β) = density-dependent term that attenuates the logarithmic rise of the cross section at very high energy

2.1.3 Stopping power

The "stopping power" (S) gives the kinetic energy loss per unit length of a particle along its trajectory. It represents the property of materials to slow down an incident ion as it passes through [7]. A convenient way to express the stopping power of a material with mass density ρ is by means of the *mass stopping power,* defined as follows:

$$\left(\frac{S}{\rho}\right)_{tot} = \frac{1}{\rho}\frac{dE_k}{dl} \tag{2.5}$$

The mass stopping power has dimension of $MeVcm^2/g$.

$(S/\rho)_{tot}$ consists of two components:

For electrons (Equation 2.6), the mass *collision* stopping power $(S/\rho)_{col}$ arises from interactions with orbital electrons of the medium (atomic excitations and ionizations). The mass *radiative* stopping power $(S/\rho)_{rad}$, results from interactions with the nucleus of the atoms (bremsstrahlung quanta production) [14].

For protons and heavier ions (Equation 2.7), the mass nuclear stopping power $(S/\rho)_{nucl}$ due to energy transfer to recoiling atoms in elastic collisions, replaces the mass radiative stopping power [15]:

$$\left(\frac{S}{\rho}\right)_{tot} = \left(\frac{S}{\rho}\right)_{col} + \left(\frac{S}{\rho}\right)_{rad} \tag{2.6}$$

$$\left(\frac{S}{\rho}\right)_{tot} = \left(\frac{S}{\rho}\right)_{col} + \left(\frac{S}{\rho}\right)_{nucl} \tag{2.7}$$

Examples of the contribution of these components to the total mass stopping power for two different ions in silicon are shown in Figure 2.1.3:

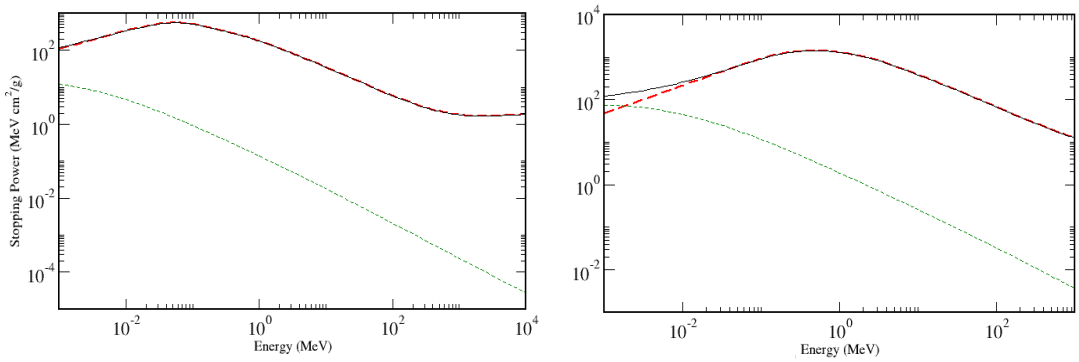

Figure 2.1.3 Total mass stopping power (solid black line), mass collision stopping power (red dashed line) and mass nuclear stopping power (green dashed line). Right: hydrogen. Left: helium ions in silicon. Adapted from [16].

2.2 Principle of operation of a silicon detector

2.2.1 Basic properties of silicon

The Timepix device is a semiconductor detector (also called solid state detector). Semiconductor materials have physical properties between conductors like metals, and insulators like polymers. This means that they have lower conductivity and lower resistivity. In the field of radiation detection, silicon (Si) is the most widely used semiconductor material [17].

Some physical properties of silicon are summarized in Table 2.2. The reported values are valid at room temperature (300 K).

Property	Si
Atomic weight	28.09
Crystal structure	Diamond
Density $[g/cm^3]$	2.329
Dielectric constant	11.9
Energy gap $[eV]$	1.12 (indirect)
Mobility $[cm^2/V-s]$	Electrons $\mu_e = 1.450$
	Holes $\mu_h = 500$

Table 2.2 Properties of silicon at room temperature. Taken from [18].

2.2.2 The p-n junction and the depletion zone

A p-n junction is created when the impurity concentration of either the p- or the n-type material is modified such that both materials have opposite electronic configurations [19]. The junction represents a discontinuity in electron density creating a net diffusion of electrons and holes from the high- to the low-density region. The effect of the diffusion is to build up a net negative space charge on the p-type side and a net positive space charge on the n-type side of the junction. The space charge creates an electric field that moderates diffusion. Once equilibrium is reached, a steady state charge distribution is achieved [19]. The stable space charge region is free of charge carriers and is called the **depletion zone** [20], as illustrated in Figure 2.2.1. The potential barrier created in the pn-junction is overcome by applying an external voltage. In this way, the junction will enable charge conduction.

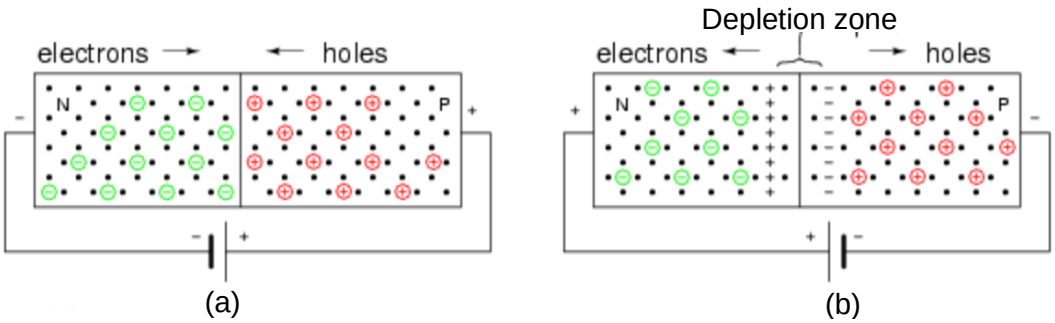

Figure 2.2.1 Silicon detector (a) forward and (b) reverse biased. Reprinted from [21].

2.2.3 Principle of operation

The principle of operation of this type of detectors can be summarized in three points:

1. First it is necessary to create an electric field in the detector. A voltage to deplete the thickness of the sensor must be applied. In the presence of an external electric field the electrons and the holes are able to move within the semiconductor material, and consequently a current may be measured.
2. Ionizing particles will create free charge carriers (electron-hole pairs) in the depletion zone. The charge carrier produced will drift to the electrodes, inducing an electrical signal proportional to the energy of the incoming radiation.
3. The produced charge carriers will move under the influence of the electric field and hence a current is induced. This current is measured.

"I hadn't been aware that there were doors closed to me until I started knocking on them".
Gertrude B. Elion

3

Material and Methods

In the present chapter, the materials used for the measurements of this thesis as well as the followed experimental and simulation methodology are described. The provided information is organized in two main parts: Section 3.1 reports materials and methods used in the experimental phase, explicitly the place at which measurements were performed (the Heidelberg Ion-Beam Therapy center), the employed sensor device (Timepix detector) and how the results were handled (data post-processing). Section 3.2 introduces the methodology followed in the Monte Carlo simulations.

3.1 Experiments

3.1.1 The HIT facility

The experiments were conducted at the *Heidelberg Ion-Beam Therapy Center* (HIT), where hydrogen (^{1}H), helium (^{4}He), carbon (^{12}C) and oxygen (^{16}O) ion beams are generated with positively charged nuclei accelerated in a two-step process. The beams mentioned above are produced using hydrogen and carbon dioxide (CO_2) gases as ion sources. Once the atoms of interest are extracted from the appropriate source, ions are accelerated up to 12% of the speed of light [22] in a linear accelerator and then directed towards a synchrotron for further acceleration. In the synchrotron the beam adopts a circular trajectory by means of six 60° magnets, reaching up to 75% of the speed of light [22]. After ions have been accelerated, the beam is focused and guided to the treatment or experimental room in vacuum tubes.

At the HIT facility there are four beam lines available, pictured in Figure 3.1.1: two treatment rooms with fixed beam line, one treatment room provided with a gantry for

rotational treatments and one experimental room with fixed beam line. The measurements for this research were performed in the experimental room.

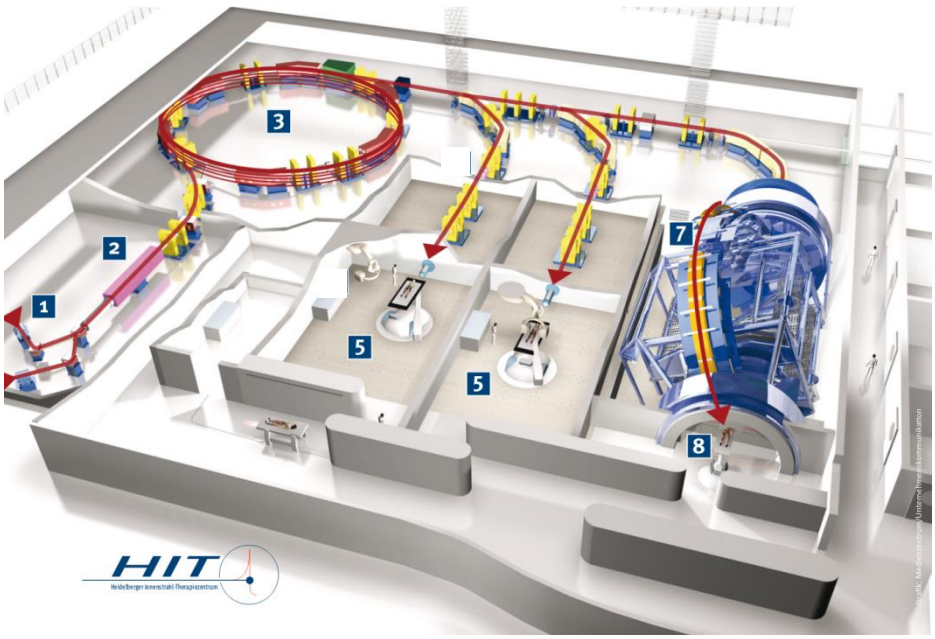

Figure 3.1.1 HIT facility: (1) Ion sources. (2) Linear accelerator. (3) Synchrotron. (5) Treatment rooms with fixed beam line. (7) Gantry. (8) Treatment room for rotational therapy. Reprinted from [22].

During the experiments all available ion species were studied and for each, four different energies were of interest, reported in Table 3.1. The largest focus F4 (defined as the beam's FWHM at the isocenter) was used in all cases and a low fluence was required. The low ion fluence was achieved by intentionally loosing particles during the extraction process, changing the angle of the first magnets. The investigated ion energies and their corresponding foci are listed below:

Ion	Energy Step	Energy [MeV/u]	Foci at isocenter (F4) [mm]
^{1}H	1	48.12	32.7
	21	70.03	24.7
	125	142.66	15.2
	255	221.06	12.6
^{4}He	1	50.57	20.6
	21	71.73	15.7
	125	143.52	11.2
	255	220.51	10.1
^{12}C	1	88.83	13.4
	21	129.79	11.8
	255	430.10	9.8
^{16}O	1	103.77	13.1
	21	152.42	11.6
	125	320.63	10.3
	205	430.32	10.1

Table 3.1 Investigated ion species with their corresponding energy and focus (at isocenter). The values were extracted from the Library of Ion Beam Characteristics (LIBC).

3.1.2 The Timepix detector

The Timepix detector shown in Figure 3.1.2 was used for the present study. It is a silicon pixelated device developed within the *Medipix2 Collaboration* [23] at CERN. Currently the Medipix family comprises six members: Medipix-1 chip, Medipix-2 chip, Medipix-2 MXR, Medipix-3 chip, Timepix (2006) and Timepix-3 chip (2016) [23]. The Timepix chip is an upgrade of the Medipix-2 chip [24] with the innovation of allowing energy deposition measurements in each pixel and a frame read-out mode.

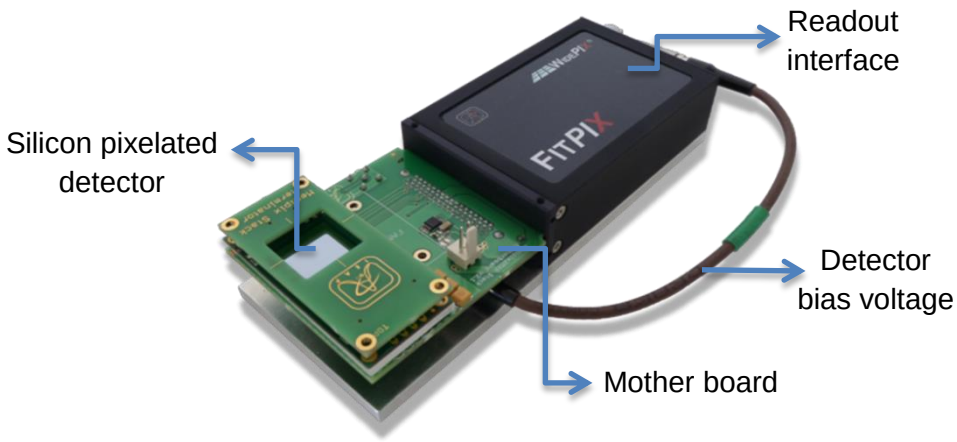

Figure 3.1.2 Timepix detector connected to the readout interface *FITPIX*. Adapted from [25].

The Timepix detector consists of three parts as depicted in Figure 3.1.3: a sensitive layer or sensor, a bonding region, and a readout chip, described below.

- **Sensitive layer:** the sensitive layer is made of silicon and has a thickness of $100\ \mu m$ covering an area of 2 cm^2. This area is divided in 256 x 256 square pixels giving a total of 65,536 pixels of 55 x 55 μm^2 area. Each pixel can be operated independently in one of four different modes.
- **Bonding region:** the sensitive layer and the readout chip are attached together by means of the so called "bump-bonding" technology. Spheres of 25 µm in diameter are welded to the sensitive layer in a ratio of 1 per pixel. This allows the independent performance of every pixel since each one has its own electronics and circuitry. These spheres are made of an alloy which is a mixture of 63% tin (Sn) and 37% lead (Pb).
- **Readout chip:** the readout chip layer is made of silicon and has a thickness of 700 µm, with the same area as the sensitive layer. It holds the circuitry of each pixel in the sensor.

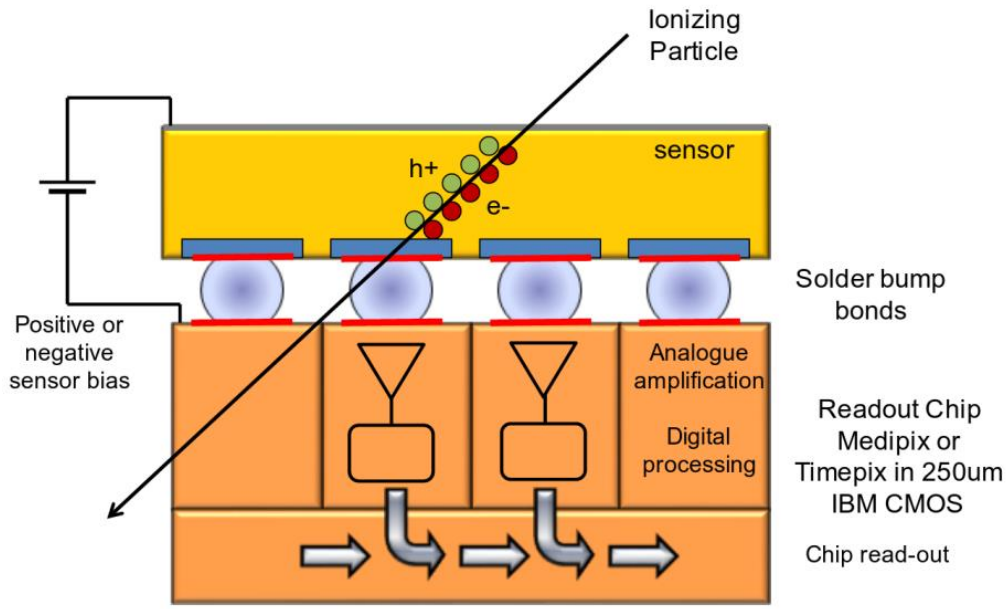

Figure 3.1.3 Cross section schematic view of the Timepix detector, showing the above mentioned three constituting regions: sensor, bounding region and readout chip. Reprinted from [26].

Each individual pixel in the readout chip can be divided in two parts: one analog and one digital, as can be seen in Figure 3.1.4.

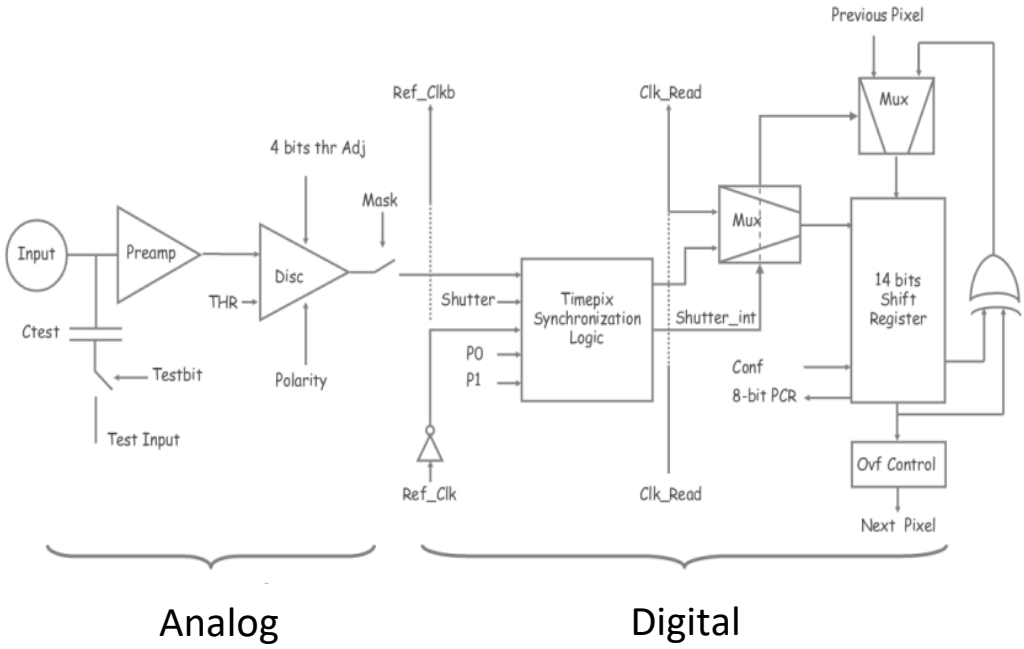

Figure 3.1.4 Analog and digital parts of the circuitry of a single pixel in the Timepix detector. Reprinted from [24]

In the analog part the pixel contains a preamplifier based on a cascaded differential CMOS amplifier [24] and a discriminator in which the threshold (*THR)* is set. The preamplifier produces a voltage step output proportional to the collected charge in the

electrode of the pixel. Then the signal is sent to the discriminator, where the comparison of the signal against the predefined threshold takes place. This threshold is set much higher than electronic noise. For the Timepix detector used in this study the threshold was equal to 5 keV. When the signal exceeds the 5 keV threshold it is sent to the digital part. Otherwise it is ignored.

In the digital part there is a reference clock (*Ref_Clk*) which can be set up to 100 MHz. There are two bits (*P0* and *P1*) available to select the operation mode of the detector according to the configuration presented in Table 3.2:

Mode	P0	P1
Counting	0	0
Time over Threshold	1	0
Time of arrival	1	1

Table 3.2 Bit configuration for the different operation modes of a Timepix detector.

The Reference Clock increases the counter in relation to the values of *P0* and *P1,* as described below.

The digital part contains a 14-bit shift register (or counter) limited to a maximum number of 11810 counts [24]. If counts go further the counter reaches an overflow regardless the operation mode in which the detector is being used.

The Timepix synchronization logic (*TSL*) controls the discriminator in the analog part of the pixel and sends the signal to the counter whenever the THR is exceeded [24]. The shift register stores all signals until the end of the frame.

Every pixel in the Timepix device can be configured to operate in three different modes, listed next and illustrated in Figure 3.1.5. In addition, there is also one bit available to operate the sensor in a fourth mode. In this mode, damaged pixels are masked, meaning that they will be “blind” to the incoming stimulus and therefore no signal will be registered.

- **Single particle counting (*Medipix mode*)**: in this operation mode, the counter increments by one every time the signal produced by an impinging particle exceeds the threshold [24].
- **Time of arrival "TOA" mode (*Timepix mode*):** when the incoming signal exceeds the threshold, the counts increase until the end of the frame.
- **Time over Threshold "TOT" mode (*Energy mode*):** when operated in this mode, energy measurements are possible [27]. In the TOT mode the counts increase continuously as long as the signal is over the threshold [24]. After the measurements, the counts (or the TOT value) can be converted into energy when an appropriate calibration is applied.

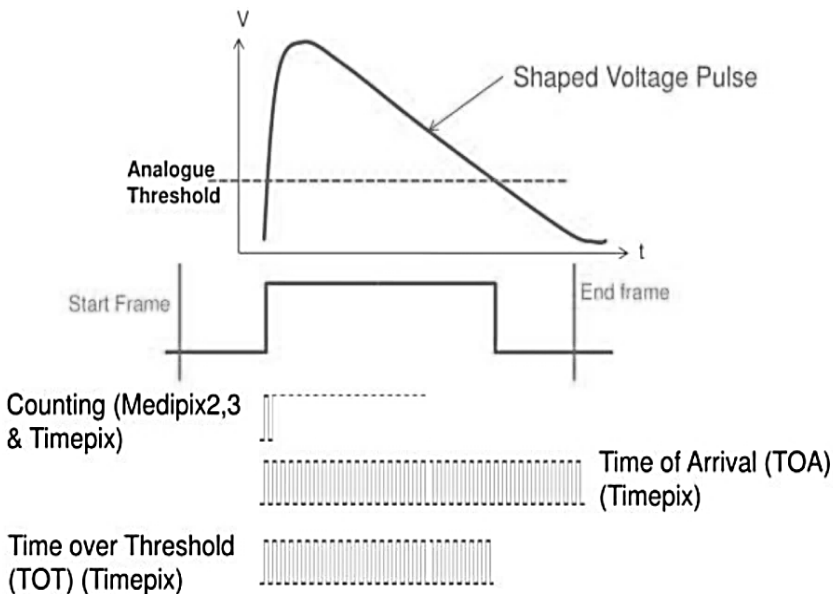

Figure 3.1.5 Operating modes of a Timepix detector showing the increase of counts. Adapted from [28].

In order to convert the cluster volume (TOT value) into energy (E) it is necessary to apply a set of calibration matrices *a, b, c* and *t* provided by the manufacturer according to the following formula:

$$TOT = aE + b - \frac{c}{E-t} \,\Big|\, pixel = 1 \ldots 65536 \qquad (3.1)$$

The calibration matrices are the result of the detector´s calibration. This procedure is done to compensate for the individual response of each pixel constituting the device. To perform the calibration the detector is irradiated with different monoenergetic gamma

sources (X-Ray fluorescence emission). Then, the obtained spectrum for every single pixel is measured independently and a calibration curve is generated, as shown in Figure 3.1.6. The employed sources for the calibration of the utilized detector and their correspondent K-alpha emission energies are: ^{26}Fe ($K_\alpha = 6.404\ keV$), ^{49}In ($K_\alpha = 24.21\ keV$), and ^{241}Am ($K_\alpha = 59.54\ keV$) [30].

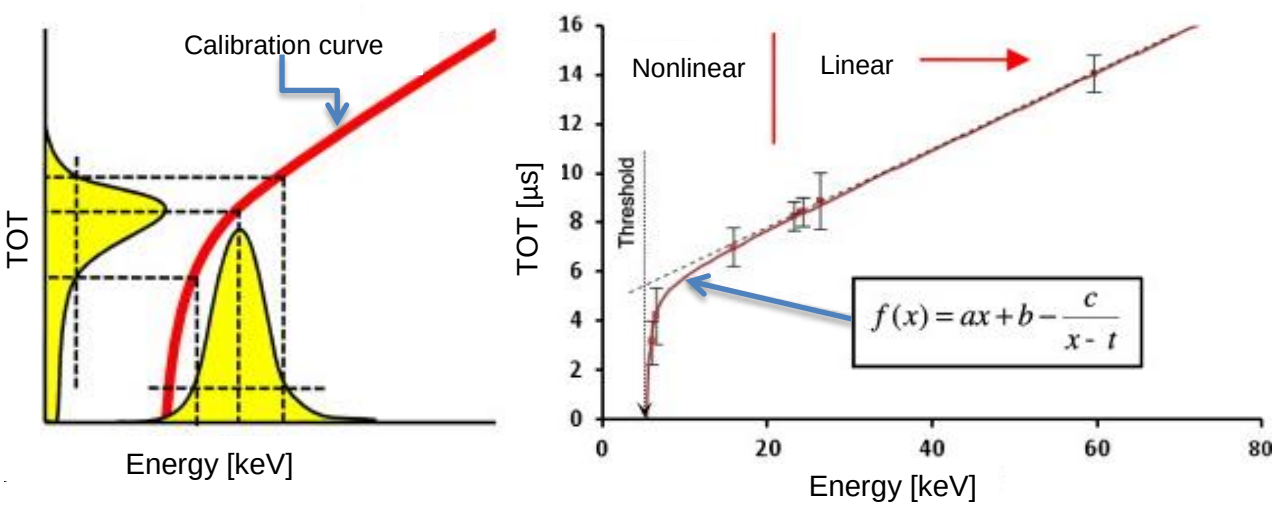

Figure 3.1.6 The calibration curve of a Timepix detector operating in TOT mode is modeled with a non-linear function that depends on four parameters a, b, c and t. Adapted from [29].

Matrices a, b, c and t contain the calibration values of each individual pixel, thus its size is 256 x 256 elements.

In this thesis, the detector was operated in TOT mode (energy mode) with a threshold equal to 5 keV, the clock set at 10 MHz and an acquisition time of 1ms.

3.1.3 Experimental set up

For the experiments, the Timepix detector *B04-W0251* was positioned at the isocenter of the experimental room at the HIT facility, approximately at 1.1 m of distance from the beam nozzle in air. The experimental array is pictured in Figure 3.1.7. In order to achieve this set up, the lasers of the room were used to position the center of the frontal face of the detector (sensitive layer) in the XY plane at the crossing point of the lasers. In the Z direction the sensitive layer was located in the isocenter. This set up ensured that the ion beam would impinge the detector perpendicularly to its sensitive area.

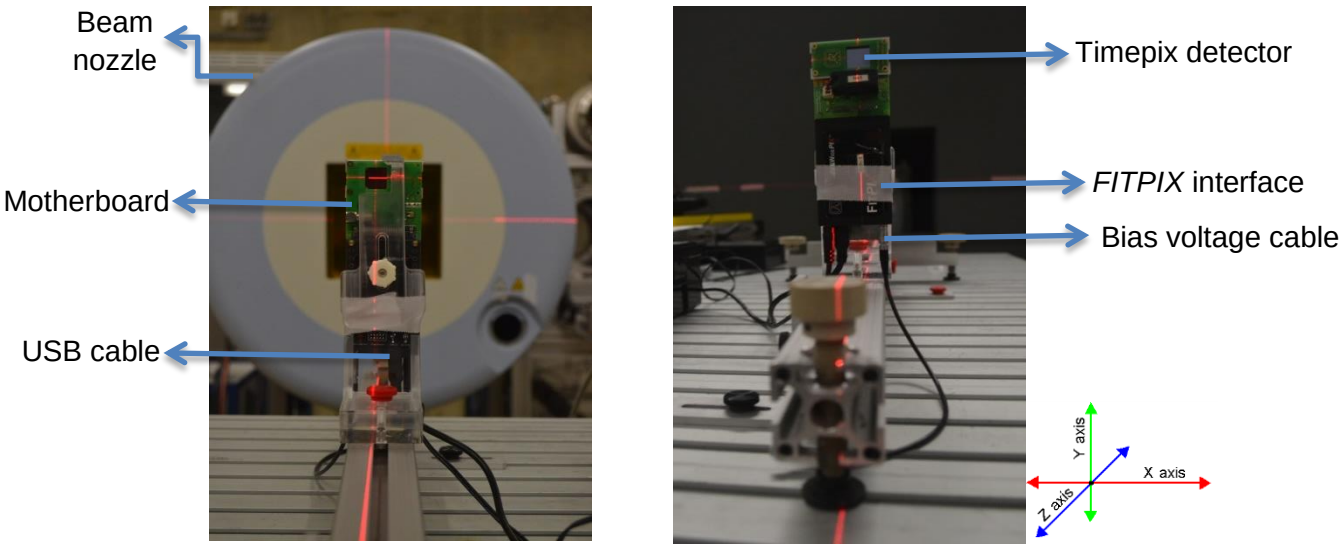

Figure 3.1.7 Back (left) and front (right) view of the experimental set up. The beam direction would be represented as an arrow coming out of the page in the left image, along the Z axis.

During the measurements, the lasers as well as the light of the experimental room were turned off to avoid detection of photons.

The sensor was operated fully depleted by applying a bias voltage of 5 V. This value for the bias voltage was calculated by making the depletion depth x_{depl} equal to the detector thickness (100 μm), according to the formula 3.2:

$$x_{depl} \approx \sqrt{\frac{2\epsilon}{qN_d}(V_0 + V_b)} \tag{3.2}$$

Where

$\epsilon =$ permittivity of silicon

$q = 1.602 \times 10^{-19}\ C$ is the elementary charge

$N_d = (0.34 \pm 0.09) \times 10^{12} cm^{-3}$ is the donor doping concentration

$V_0 =$ build-in voltage

$V_b =$ bias voltage

The detector was attached to a motherboard that allowed the connection between the detector and the USB readout interface *FITPIX*, which stands for *Fast Interface for*

Timepix pixel detectors. *FITPIX* was also connected via USB 2.0 to a computer inside the experimental room.

For all measured ion types and initial energies, attention has been put on keeping low particle fluence (even below the lowest therapeutically used fluence), yet a minimum of 1×10^5 *ok clusters* was achieved in each measurement. This reduction in particle fluence was achieved during the ion extraction stage with support of the technicians at HIT. The desired fluence was chosen visualizing acquisition frames by means of the *Pixelman* graphic user interface.

The software package *Pixelman* version 2.2.3 enabled the setting and adjustment of measurement parameters of the detector such as the bias voltage, operation mode, acquisition time and reference clock. This software also allowed visualizing and storing the measured data in ASCII files.

The obtained ASCII files contained the following information per pixel:

[*x coordinate, y coordinate, value of interest, 0*]

being the TOT value the “value of interest” since the detector was operated in energy mode. Figure 3.1.8 gives an example of a typical output file obtained with *Pixelman* in frame format:

```
Frame 1 (1509893901.7403338 s, 0.001 s)
[28, 103, 3951, 0]

Frame 2 (1509893901.7645466 s, 0.001 s)
[98, 50, 63, 0] [99, 50, 103, 0] [100, 50, 63, 0] [100, 51, 375, 0] [101, 51, 15, 0] [101, 52, 26, 0] [100, 52, 498, 0] [99, 52, 2810, 0] [98, 52, 623,
[15, 57, 25, 0]
[73, 57, 32, 0]
[60, 210, 1926, 0] [61, 210, 2061, 0]
[203, 246, 16, 0] [204, 246, 49, 0] [205, 246, 30, 0] [205, 247, 366, 0] [206, 247, 33, 0] [206, 248, 59, 0] [205, 248, 1150, 0] [204, 248, 2486, 0] [
[242, 248, 3959, 0]

Frame 3 (1509893901.7838776 s, 0.001 s)
[116, 41, 7, 0]
[217, 41, 321, 0] [218, 41, 3629, 0] [219, 41, 56, 0] [219, 42, 240, 0] [218, 42, 2664, 0] [217, 42, 452, 0]
[120, 63, 42, 0] [121, 63, 85, 0] [122, 63, 60, 0] [122, 64, 515, 0] [123, 64, 44, 0] [123, 65, 63, 0] [122, 65, 893, 0] [121, 65, 2808, 0] [120, 65, 
[186, 89, 3382, 0] [187, 89, 1597, 0]
[148, 101, 49, 0] [149, 101, 168, 0] [150, 101, 125, 0] [151, 101, 33, 0] [151, 102, 88, 0] [150, 102, 1462, 0] [149, 102, 2224, 0] [148, 102, 180, 0]
[125, 109, 36, 0]
[178, 146, 30, 0] [179, 146, 6, 0] [179, 147, 238, 0] [180, 147, 28, 0] [180, 148, 57, 0] [179, 148, 1162, 0] [178, 148, 2735, 0] [177, 148, 311, 0] [
```

Figure 3.1.8 Output file obtained with the *Pixelman* software for a measurement with the Timepix detector in energy mode. The data is given in frames: every horizontal line represents one cluster and the information given in brackets represents one pixel. For instance, Frame 2 consists of 6 clusters (6 horizontal lines). Within the same frame, cluster number 4 consists 2 pixels (2 brackets).

Before going further with the data analysis it was necessary to extract the numbers by eliminating all the letters and punctuation signs and to re-arrange the information in appropriate columns. C++ routines developed in the group were used for that. Once this has been done, the measurement's information is ready to be processed in MATLAB®, The MathWorks, Inc., Natick Massachusetts, US.

3.1.4 Data post-processing

After data acquisition three steps had to be performed before obtaining the energy deposition curves. The purpose of these steps was to keep only "clean" information from primary particles. The post-processing steps consisted in the rejection of:

- Overlapping clusters.
- Spatially cropped clusters.
- Clusters produced by secondary radiation.

The mentioned filters are described next.

When two or more particles arrive to the sensor in close vicinity, an overlapping zone is created, as depicted with the label "Overlap" in Figure 3.1.9. Overlaps can be detected by analyzing the number of local maxima per cluster. To accomplish this, local maxima was defined as a pixel value equal or bigger than its adjacent pixels and bigger than 20% of the absolute maximum [31]. If two or more local maxima were found in a cluster, that cluster was rejected.

Particles arriving to the sensitive area of the detector near its physical border would be partially detected by the device ("Spatially cropped cluster" in Figure 3.1.9). Hence, a fraction of the energy deposition in the sensor would be missed. Because of this, spatially cropped clusters were removed. To do this filtering, an artificial margin inside the detector was defined. Clusters that had their center of mass inside the margin were rejected. To create the mentioned border, 6 pixels to the border criteria was used. This quantity was chosen after analyzing the data with the largest clusters (^{16}O ions with the lowest initial energy).

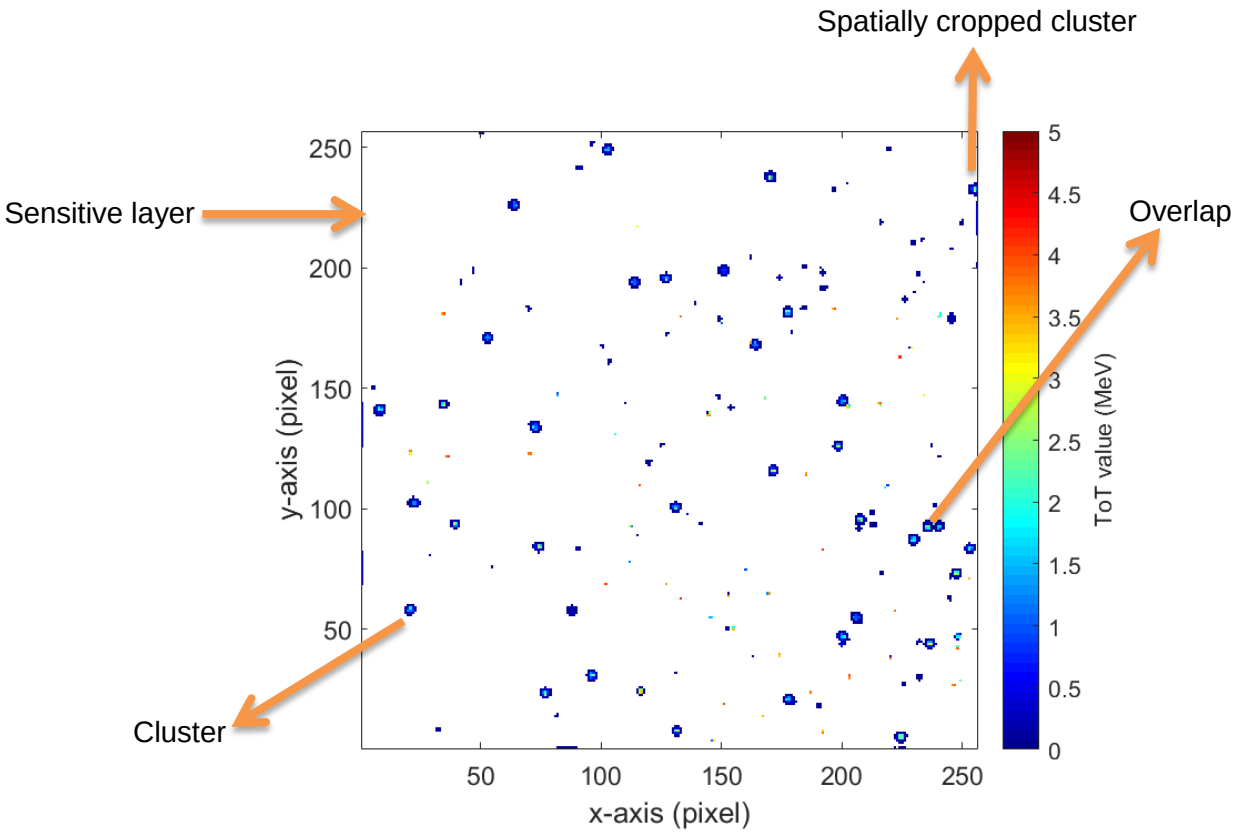

Figure 3.1.9 Frame acquired with the lowest primary beam energy of ^{16}O ions. Here, the sensitive layer of Timepix with the generated clusters can be observed. Also, an overlapping region and a spatially cropped cluster can be found in the right zone of the sensor.

To keep information produced by primary ions only, a cut in the cluster size was carried out. The cut limit was chosen by visually analyzing 2D plots of cluster size vs. cluster volume (see Results chapter). In these plots, it was possible to distinguish (based on the color code) a region of decreased – increased frequency along the cluster size axis, from small to large sizes. The cut was chosen as the cluster size in which the increase in frequency began.

3.2 Monte Carlo simulations with FLUKA

3.2.1 The FLUKA code and the physical models implemented in the simulations

The validation of the experimental data was performed using the Monte Carlo code FLUKA, version 2011.2c.6. FLUKA has been developed as a general purpose Monte

Carlo code [32] that models the interactions of various particles over a wide range of energy.

The following physical settings were defined for all the simulations:

- HADROTHERAPY: this option allows transporting low-energy neutrons down to thermal energies, activates delta ray production with a pre-defined threshold (100 keV by default) and sets particle transport threshold at 100 keV. The threshold for the delta ray production was modified to 10 keV.
- PHYSICS: when implemented, it allows the change of FLUKA default values for the coalescence and evaporation processes [36]. For the latter process the new fragmentation model is activated, making possible to simulate the evaporation of fragments up to A=24 [36].

3.2.2 Simulation of the detector

FLUKA uses the so-called combinatorial geometry. This means that every object in the simulation will be the result of boolean operations over basic geometric objects or “bodies”. The operations involved might be either intersection (I), union (+) or difference (-), as exemplified in Figure 3.2.1. Some examples of available bodies are: rectangular parallelepipeds (RPP), planes (XY, YZ, and XZ), cylinders and spheres.

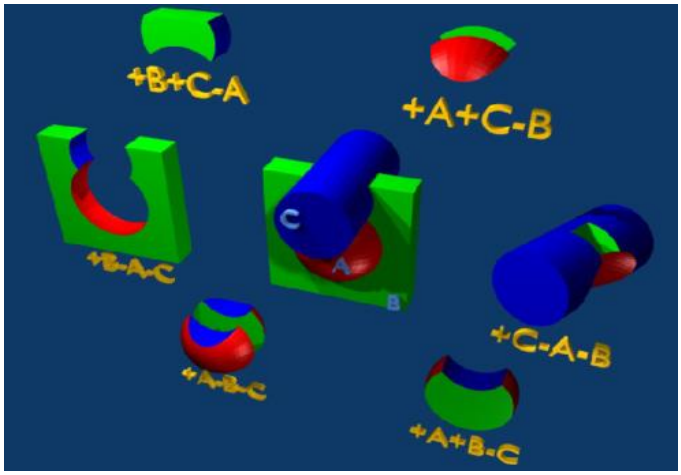

Figure 3.2.1 Region construction in FLUKA, based on combinatorial geometry. Reprinted from [33].

In order to simulate the sensitive layer and the readout chip of the Timepix detector, displayed in Figure 3.2.2, one RPP and two XY planes were used. The created regions were assigned with the silicon material predefined in FLUKA, with the following physical properties: A=28.0855, Z=82, mass density ρ= 2.329 g/cm^3.

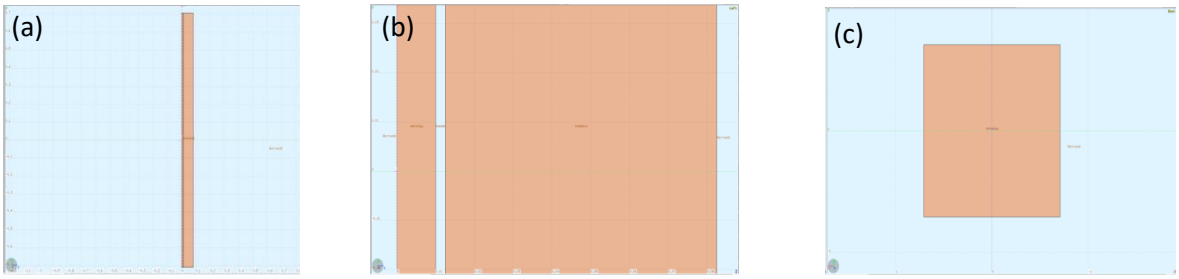

Figure 3.2.2 (a) Lateral view of the detector as simulated in FLUKA. (b) Zoom of the view in (a) showing the sensitive layer of 100 µm and the readout chip of 700 µm, both made of silicon (in orange). (c) Frontal view of the detector with an area of 2 cm^2. The surrounding material (in blue) represents the air in the experimental room.

Each sphere of the bump-bonding region was simulated with the appropriate dimensions (25 µm diameter) and composition (see 3.1.2). The whole geometry of the experimental set up was simulated inside a special non-physical material called "*Blackhole*" (see Figure 3.13), which has a mass number A=0, Z=0 and a mass density of 0 g/cm$^{3.}$ The presence of this region in FLUKA is mandatory in order to guarantee the end of the simulations. Otherwise the Monte Carlo code would follow each particle in an endless run. The *blackhole* has two main properties: no interactions may take place in it and every particle reaching this material is immediately excluded (since this moment) from the particle transport simulation.

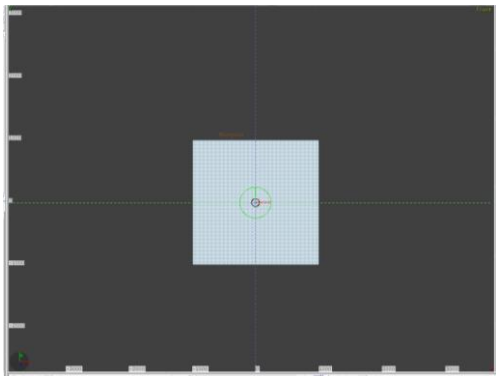

Figure 3.2.3 The blackhole region (in black) contains the simulated geometry to ensure the end of the runs.

3.2.3 Simulation of the ion beam

Two methods for the simulation of the ion beams were applied:

- By means of **phase space files (PS)**.
- By **simulating** the equivalent to the water thickness of the **Beam and Application Monitoring System (BAMS),** present in the beam line.

Both approaches will be described next.

The HIT beamline was modeled in a former work by Tessonier et al. via Monte Carlo simulations with the FLUKA code version 2011.2c [34]. This research resulted in the creation of so-called phase space files for all the ions, energies and foci available at HIT. The phase space was validated against measurements of depth and lateral dose profiles in a water phantom [34]. The PS characterize the beam on a plane perpendicular to its propagation at a defined position along the beam path by describing the charge, mass, energy, coordinates and direction cosines of every crossing particle (primary and secondary) [34] and are accessible to support measurements of external users upon request.

To simulate the beam with the PS approach, the SOURCE setting enabled the use of an external routine that called the chosen PS files. The used PS corresponded to foci F4 for each ion and initial energy of interest.

In the BAMS approach, two different settings were needed instead of SOURCE: BEAM and BEAMPOSit. With BEAM it was possible to set the type of particle, energy, divergence, profile and statistical weight [35] of the ion beam.

- Particle options include protons, triton, deuteron, helium, and heavy-ions among others. When simulating ^{12}C and ^{16}O ion beams the selected particle type was HEAVYION and the additional setting HI-PROPErt had to be activated to specify the desired particle properties.
- The energy can be given either by average momentum in [GeV/u] or average kinetic energy in [GeV].
- Divergence could be set as the width of a rectangular-like angular distribution or as the FWHM of a Gaussian-like angular distribution.

- The beam momentum spread could correspond to a rectangular-like (GeV/c) or a Gaussian-like (FWHM) distribution.

With BEAMPOSit the point at which radiation transport starts was set. Here it was possible to select the exact coordinate (value along X, Y and Z axis) and direction (positive or negative) of the ion beam.

In addition to the settings described above, a new region representing the BAMS had to be included. This region was created by means of a RPP placed in air with WATER as assigned material. The simulated BAMS had a thickness of 0.142 cm. The starting point of the ion beam was defined in vacuum to achieve a detailed geometry simulation. Therefore, the foci in vacuum instead of the foci at the isocenter were used. Figure 3.2.4 pictures the exact BAMS approach geometry.

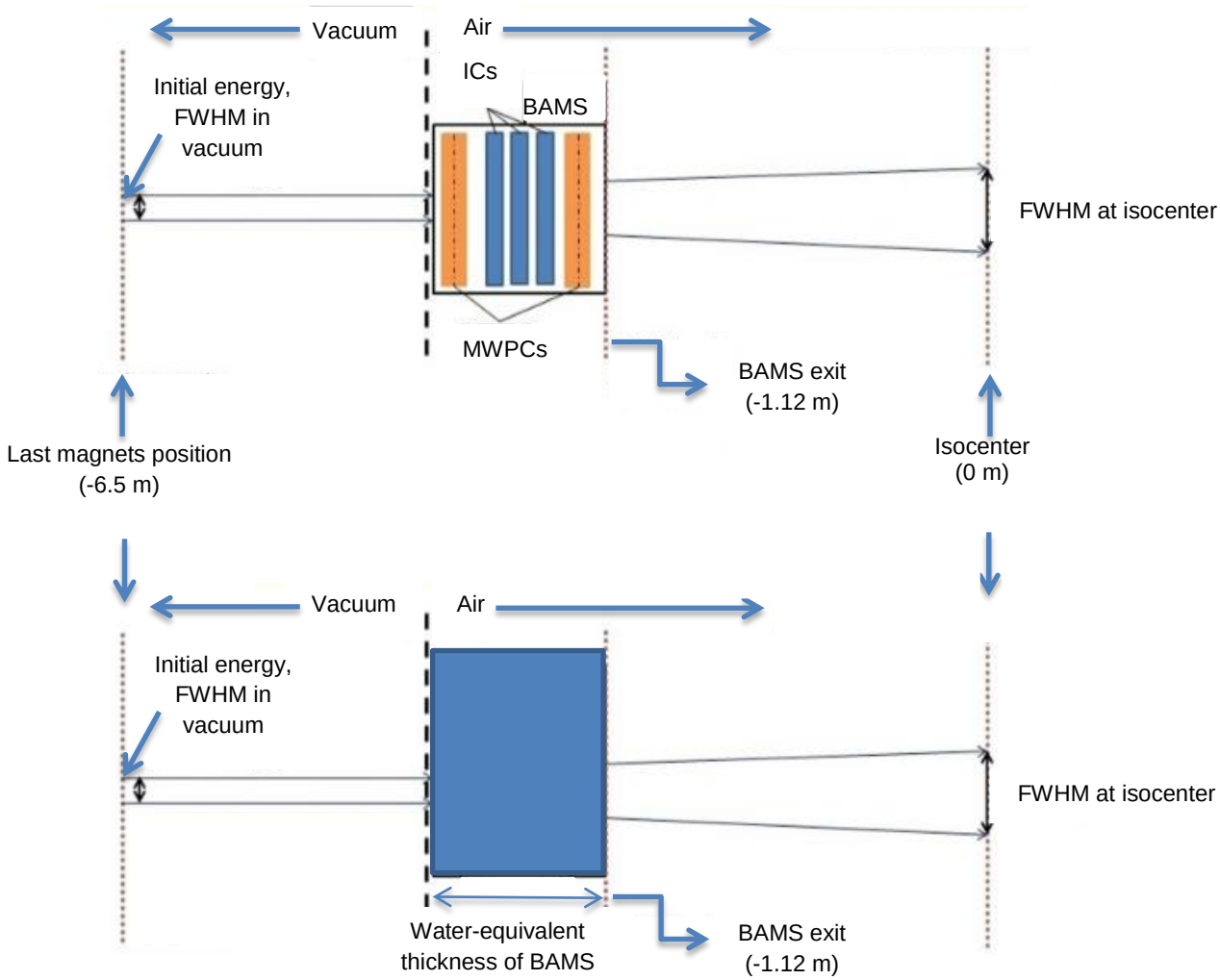

Figure 3.2.4 Upper panel: geometry of the beamline as simulated in [34]. As shown, the BAMS consists of two multiwire proportional chambers (MWPCs) and three ionization chambers (ICs). This is the last component inside the beam nozzle. Lower panel: implemented geometry in MC BAMS method to simulate the ion beam. The BAMS was simulated as a water parallelepiped in air. Adapted from [34].

"We know very little, and yet it is astonishing
that we know so much,
and still more astonishing that so little knowledge
can give us so much power".
-Bertrand Russell

4 Results

In this chapter, the obtained results from both, experiments and Monte Carlo simulations using a 100 μm thick Timepix detector are presented. In Section 4.1, raw data characteristics as well as the effect of the post-processing steps, described in Chapter 3, are shown. In Section 4.2, (plots of) measured and simulated energy deposition for ^{1}H, ^{4}He, ^{12}C and ^{16}O ions with four different primary beam energies are presented, in addition to the correlation between mean energies deposited and the FWHM of each spectrum. Furthermore, the results are compared to a 300 μm thick Timepix detector. All the graphs presented in this chapter have been generated using the MATLAB® software (Mathworks, Nattick, MA, USA) version 9.2.0 R2017a with academic license number 346640.

4.1 Experimental Results

In this section the results from measurements using a detector with a fully depleted 100 μm thick silicon sensor are presented. The detector parameters used throughout the experiments as well as the experimental set up can be found in Chapter 3. The dead time of the detector during the experiments was of the order of 0.0025 s.

4.1.1 The raw data

The first analyzed raw data characteristic was the cluster size. Histograms of cluster size for the four ion species and for each primary beam energy are presented below, together with their corresponding energy deposition histograms. In these histograms, an area normalization has been applied.

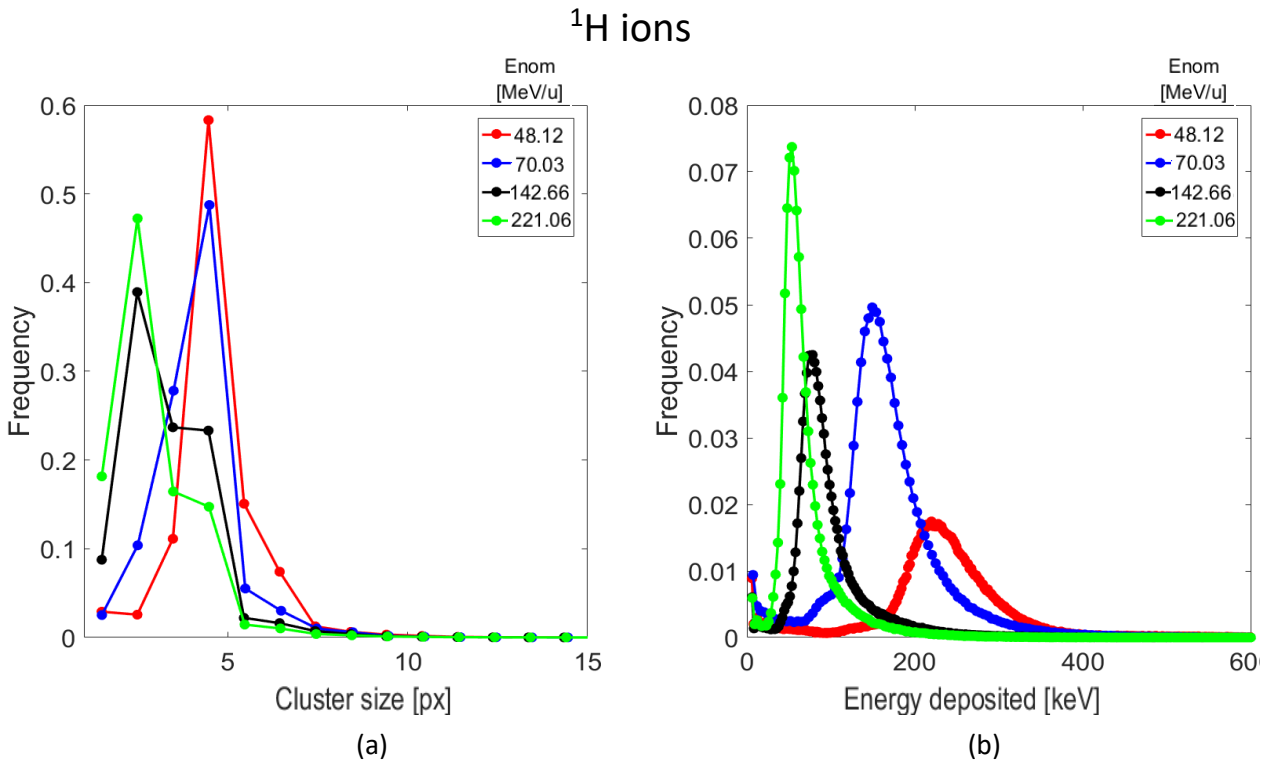

Figure 4.1.1 Histogram of the cluster size (a) and energy deposited (b) of raw data for ^{1}H ions with four different initial energies. More than $3x10^{5}$ clusters per initial energy are plotted.

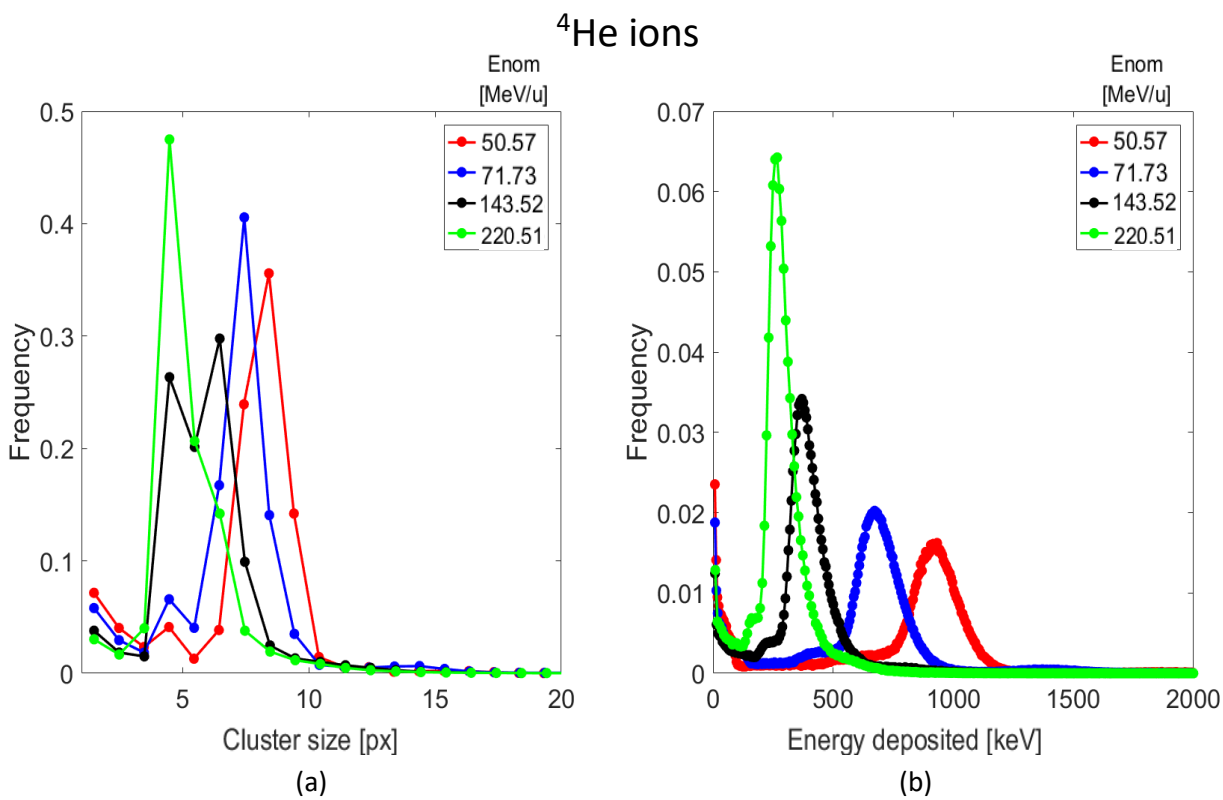

Figure 4.1.2. Histogram of the cluster size (a) and energy deposited (b) of raw data for ^{4}He ions with four different initial energies. More than $2x10^{5}$ clusters per initial energy are plotted.

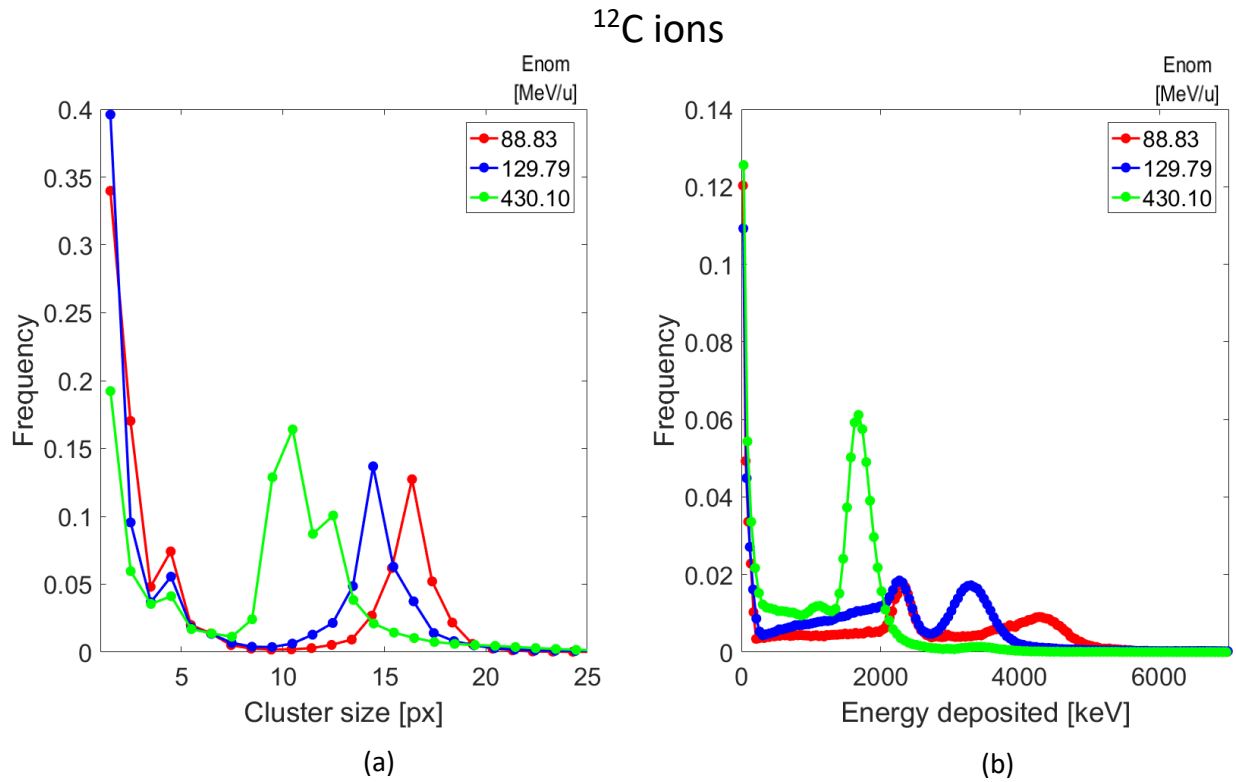

Figure 4.1.3. Histogram of the cluster size (a) and energy deposited (b) of raw data for ^{12}C ions with three different initial energies. More than $2x10^5$ clusters per initial energy are plotted.

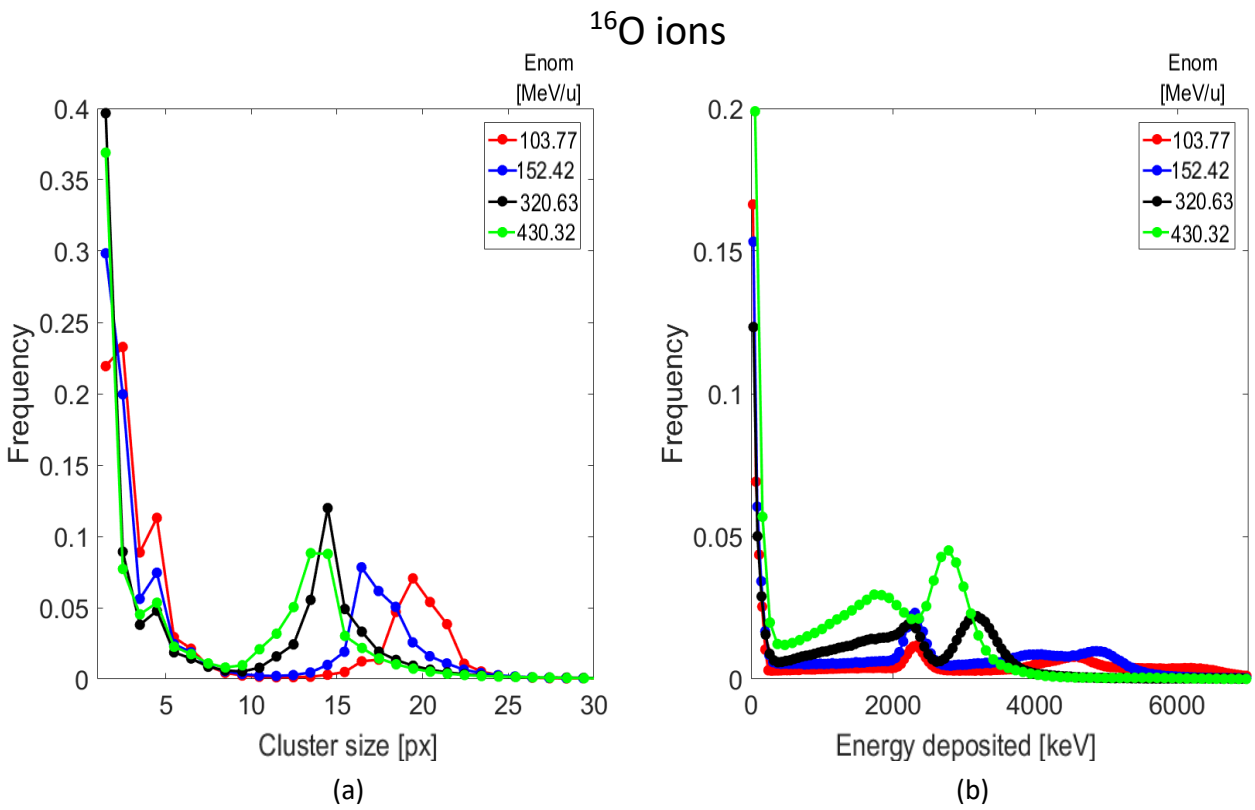

Figure 4.1.4. Histogram of the cluster size (a) and energy deposited (b) of raw data for ^{16}O ions with four different initial energies. More than $9x10^5$ clusters per initial energy are plotted.

In the preceding cluster size histograms, a two-peak pattern is visible for heavy ions: the first peak appeared centered at small cluster sizes, generally covering a range in size between 1 and 5 pixels. The second peak was centered at larger cluster sizes. The first peak, produced by secondary radiation, showed higher frequencies than the second peak for ^{12}C and ^{16}O ions. In contrast, ^{4}He and ^{1}H ions exhibited 1 peak distributions.

It was also noticed that the range in size covered by the clusters belonging to the second peak increased as the charge of the ion increased. For instance, if the lowest energy step available is considered (red lines in Figures 4.1.3 and 4.1.4), the second peak for ^{12}C ions was centered at 17 pixels and for ^{16}O ions at 20 pixels.

Conversely, within the same ion type the cluster size where the second peak was centered decreased with increasing primary beam energy. Let us take ^{16}O ions for this example: the center of the second peaks were located at 20, 17, 16 and 14 pixels for energy steps 1, 21, 125 and 205, respectively (corresponding to the red, blue, black and green lines in Figure 4.1.4).

Similarly, the two-peak pattern was visible in the energy deposition histograms of ^{4}He, ^{12}C and ^{16}O ions, and likewise, the first peak appeared at low deposited energies and showed higher frequencies for the heavier ions. The observed shape in the energy deposited spectra is due the following contributions:

- Secondary radiation (first peak, in the low energy deposition region).
- Primary ions (second peak, in higher energy deposition values).

Particularly, for ^{12}C and ^{16}O ions the energy deposition curves of raw data presented a gradual fall-off in the upper tail of the spectrum. The lower tail exhibited “sub-peaks” reaching lower frequencies than the main two peaks of the spectrum.

4.1.2 Data post-processing

As explained in Chapter 3, three post-processing steps were applied to the measured raw data in order to keep information only from single primary ions and to have as complete and “clean” as possible registered events. In this regard, clusters produced by secondary radiation or clusters produced by primary ions that were somehow altered,

were deleted. The post-processing steps aimed to reject overlapping and spatially cropped clusters, and clusters produced by secondary radiation.

Each post-processing step reduced the amount of available clusters for further analysis by different fractions. To give an overview of the magnitude of such reduction, a table reporting the percentage of rejected clusters is presented next (Table 4.1). This table includes the final number of clusters used for the analysis of the energy deposition. The rejection percentage was calculated based on the quantity shown in the column “Unprocessed clusters”, fixing the number of initial clusters to be the 100% in order to show the impact of each post-processing step on the total acquired raw data.

The fraction of excluded clusters varied between 13.1% and 80%, as shown in Table 4.1. ^{1}H ions with the lowest initial energy were the particles with the fewest number of removed clusters, retaining almost 87% of the measured events for further analysis. This was attributed to the lack of secondary ions for ^{1}H beams. In contrast, ^{16}O ions with the lowest initial energy were the particles with the highest number of discarded clusters, retaining only 20% of the total detected clusters. The excluded clusters accounted for more than 10% of the initial amount of available data. However, it was possible to analyze more than 10^5 clusters per ion type and primary beam energy, except for ^{12}C ions of the lowest initial energy for which 66,479 clusters remained to investigate the deposited energy spectrum.

The cut in cluster size was the filter with the highest rejection rate, producing a larger impact for ^{12}C and ^{16}O ions. It was also observed that the rate of rejection of the filtering step number 1, which corresponds to the removal of overlapping and temporally cropped (at the end of a frame) clusters, increased for ions with larger mass, i.e., ^{12}C and (even more) ^{16}O ion beams. The latter two ion species were more likely to produce overlapping clusters than ^{4}He and ^{1}H ion beams. This was due to the fact that ^{12}C and ^{16}O beams produced larger clusters than ^{4}He and ^{1}H beams, and also because of the higher fluence. The rejection rate produced by the second post-processing step, aiming to remove the spatially cropped clusters, was on average higher for ^{12}C and ^{16}O ions. Within the same ion type, more spatially cropped clusters were found in beams with the lowest primary beam energy since the produced clusters exhibited a larger size.

Ion	Energy step	Unprocessed clusters	Rejected clusters after post-processing step 1 [%]	2 [%]	3 [%]	Final amount of clusters
^{1}H	1	319,037	1.9	10.6	13.1	277,411
	21	522,144	2.0	9.9	0.0	470,504
	125	464,838	2.6	8.8	0.0	424,083
	255	391,511	2.1	7.1	0.0	363,741
^{4}He	1	239,843	3.6	12.7	28.2	172,290
	21	580,689	4.5	12.3	20.1	463,993
	125	321,959	4.3	10.5	15.5	272,151
	255	368,078	4.3	9.4	13.6	318,031
^{12}C	1	259,297	5.5	11.3	74.4	66,479
	21	888,271	6.2	12.0	70.3	263,922
	255	592,629	7.4	12.9	44.7	327,475
^{16}O	1	1,027,967	7.1	13.3	80.0	205,332
	21	985,312	6.9	13.0	76.8	228,623
	125	1,720,892	6.3	11.3	69.0	533,651
	205	2,404,353	6.8	13.1	68.0	770,608

Table 4.1 Percentage (with respect to the total) of overlapping and temporally cropped at the end of a frame clusters (step1), spatially cropped clusters (step 2) and clusters belonging to overshoots, temporally cropped at the beginning of a frame and secondary particles (step3) removed from raw data. All the ions and initial energies analyzed in this work are presented.

The selection of the benchmark used in the cluster size filter was chosen by means of 2D histograms of cluster size vs. cluster volume (see Section 3.2 for more details). As mentioned, two pronounced peaks in the cluster size axis could be distinguished in the raw data of heavy ions. Thus the aim of the cut in size was to remove the peak located in small cluster sizes since it is produced by the contribution of the overshoot effect, by clusters that impinged the detector before an acquisition has started, and by secondary particles losing low energy in the sensitive layer of the detector. The applied cuts on cluster size (lower threshold) are summarized in Table 4.2.

Ion	Energy step	Cut in cluster size [px]
^{1}H	1	2
	21	-
	125	-
	255	-
^{4}He	1	5
	21	3
	125	3
	255	3
^{12}C	1	10
	21	9
	255	6
^{16}O	1	14
	21	12
	125	9
	205	9

Table 4.2 The selected lower threshold in cluster size was different between ion types and beam energies.

For protons from energy step 21 on, it was not possible to apply the cluster size filter because the searched pattern was not visible in these data sets. This was due to the lack of secondary radiation in proton beams and to the fact that photons and electrons can be in the same peak as ^{1}H ions.

A visual representation of how raw data was affected from one post-processing step to the other is provided by 2D histograms of cluster size vs. cluster volume, as displayed below in Figure 4.1.5. These plots were made for each ion type and primary beam energy, but only the graphs for 88.83 MeV/u ^{12}C ions (energy step 1) are shown next for the sake of the extension of this chapter.

In the upper left panel of Figure 4.1.5 all clusters were included, illustrating how raw data was composed in terms of size of the clusters and its corresponding volume. The size of a cluster was determined by the number of pixels belonging to it while its volume is the result of the sum of the value of each pixel comprising the cluster. In the upper right panel, on which overlapping clusters were rejected, it is possible to distinguish how the zone of big clusters with large volume (corresponding to the overlaps) is almost gone compared to the situation observed in the raw data plot. Similarly, a reduction in the amount of temporally cropped clusters at the end of the frame, which are clusters that for a fixed cluster size (particularly around 16 pixels) exhibit degraded cluster volumes,

is visible. In the lower left panel, on which the spatially cropped clusters were removed from the measured data, it is possible to observe a decrease in frequency in the region of small clusters (around 5 and 13 pixels) with reduced volume (below 2 MeV). Finally, the cut in cluster size is shown in the lower right panel, depicting that clusters smaller than 10 pixels were deleted. This means that the final result is a clean sample of primary ions only.

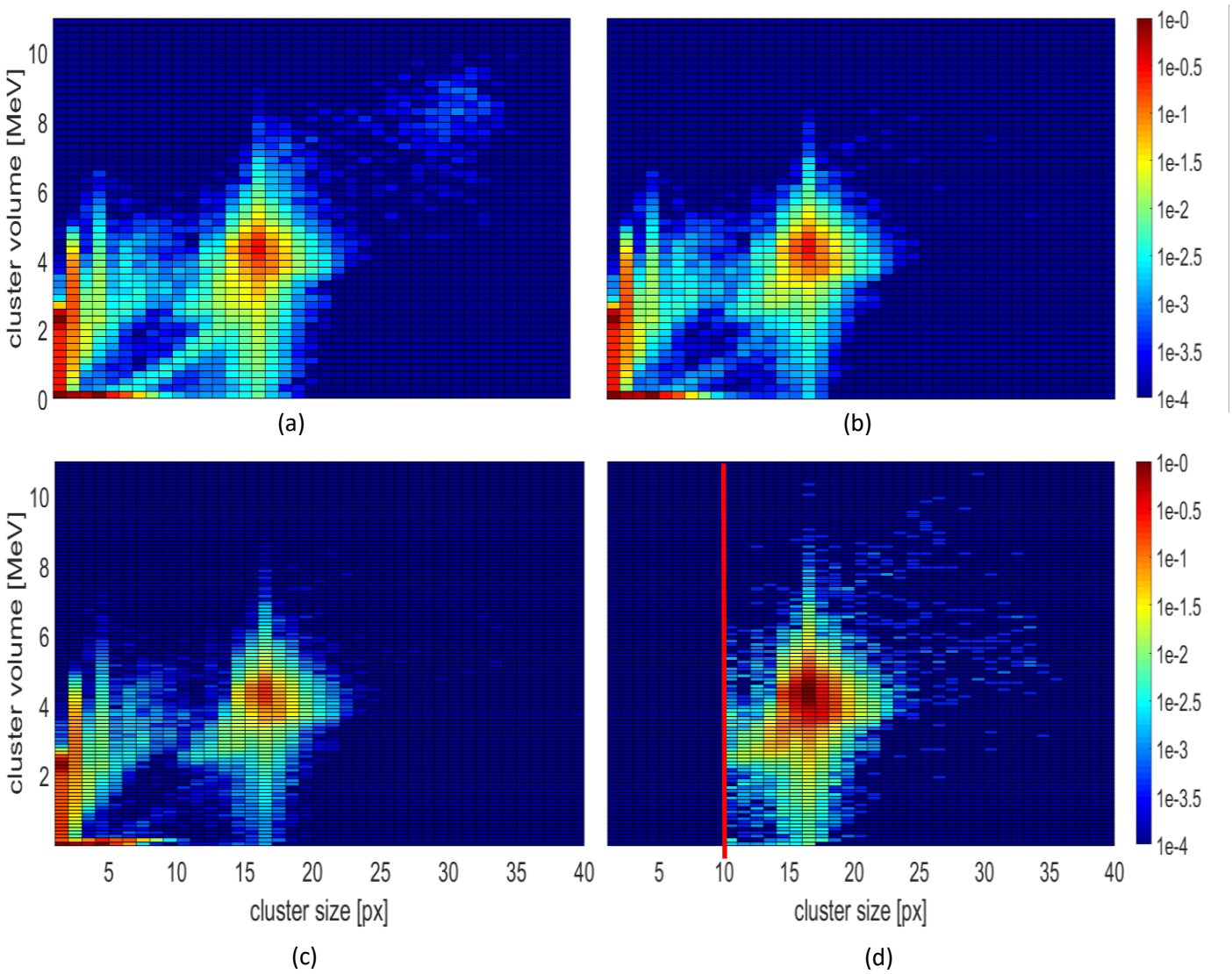

Figure 4.1.5. Illustration of single data processing steps on the distribution of clusters in size and volume for ^{12}C of 88.83 MeV/u. (a) Raw data. (b) Raw data after the removal of overlapping and temporally cropped clusters. (c) The data shown in (b) after spatially cropped clusters were rejected. (d) The data shown in (c) after the cut in cluster size was applied. The red vertical line depicts the used lower threshold in the size cut (10 pixels in this example). The logarithmic color scale on the right of the histograms indicates the frequency normalized to the maximum.

4.2 Comparison of deposited energy in experimental data and simulations

In the following pages, the resulting energy deposited spectra of primary ions from measurements and from Monte Carlo simulations are presented. For the experimental data the post-processing steps allowed to keep information from primary particles only, while for the simulated data it was possible to select which particles to track in advance. The simulation of the beam was done using two different approaches, namely the phase space (PS) and the BAMS methods, as commented in Chapter 3. Therefore both results are included in the next graphs.

4.2.1 Spectra of deposited energy in a 100 µm thick sensor

The spectra of deposited energy by primary ions in the 100 µm silicon sensor of the utilized *B04-W0251* Timepix detector are shown in Figures 4.2.1- 4.2.4.

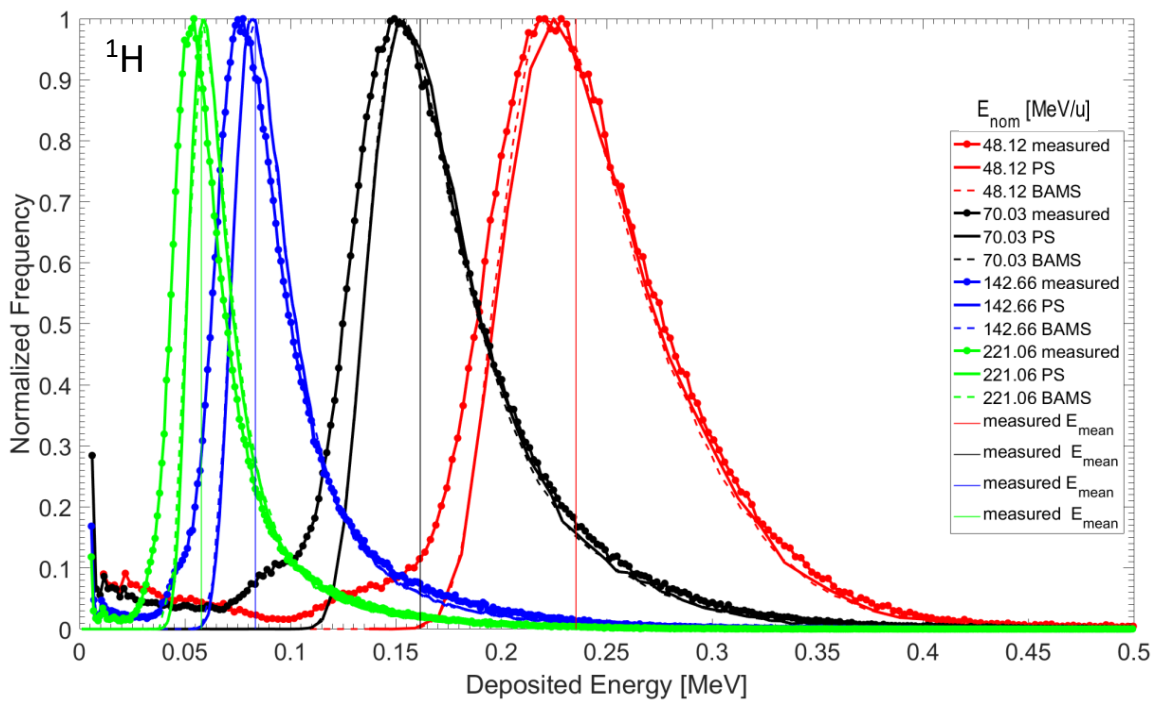

Figure 4.2.1. Measured (solid lines with markers) and simulated (solid and dashed lines) energy deposition distribution for ^{1}H ions of four different primary beam energies in a 100 µm thick silicon sensor. For the simulation of the ion beam phase space files (PS) or corresponding to the water equivalent thickness of the BAMS were used. Vertical lines show the location of the measured mean deposited energy. Each histogram was normalized to its maximum.

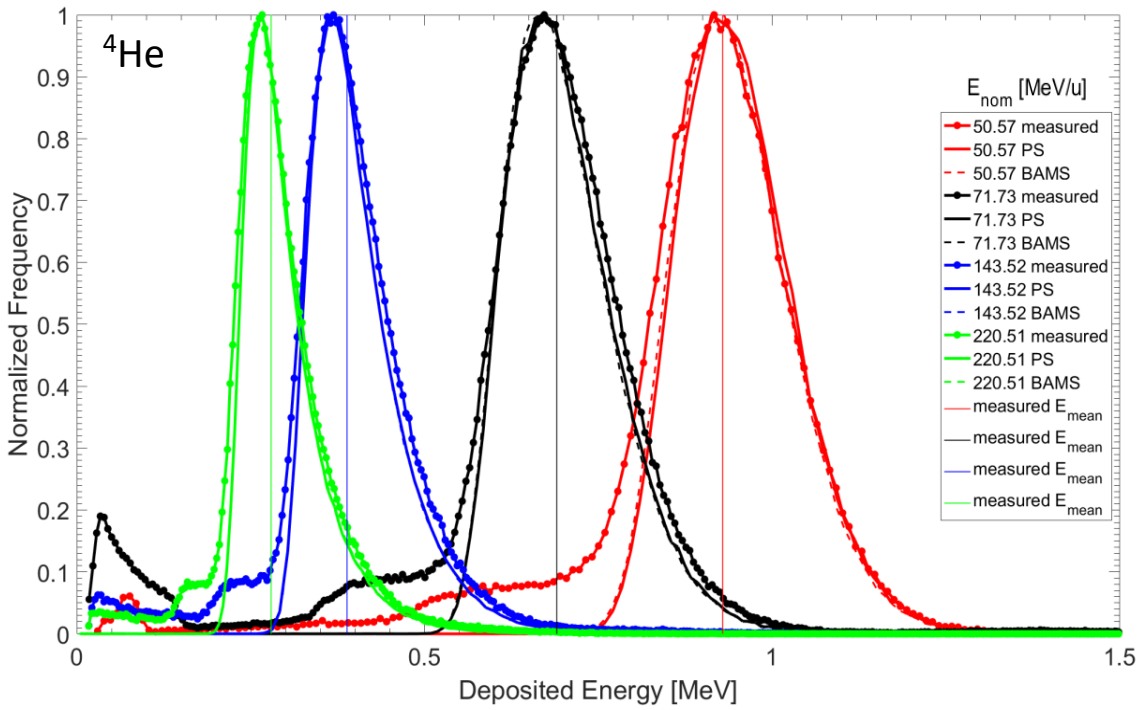

Figure 4.2.2. Measured (solid lines with markers) and simulated (solid and dashed lines) energy deposition distributions for ^{4}He ions of four different primary beam energies in a 100 µm thick silicon sensor. For the simulation of the ion beam phase space files (PS) or corresponding to the water equivalent thickness of the BAMS were used. Vertical lines show the location of the measured mean deposited energy. Each histogram was normalized to its maximum.

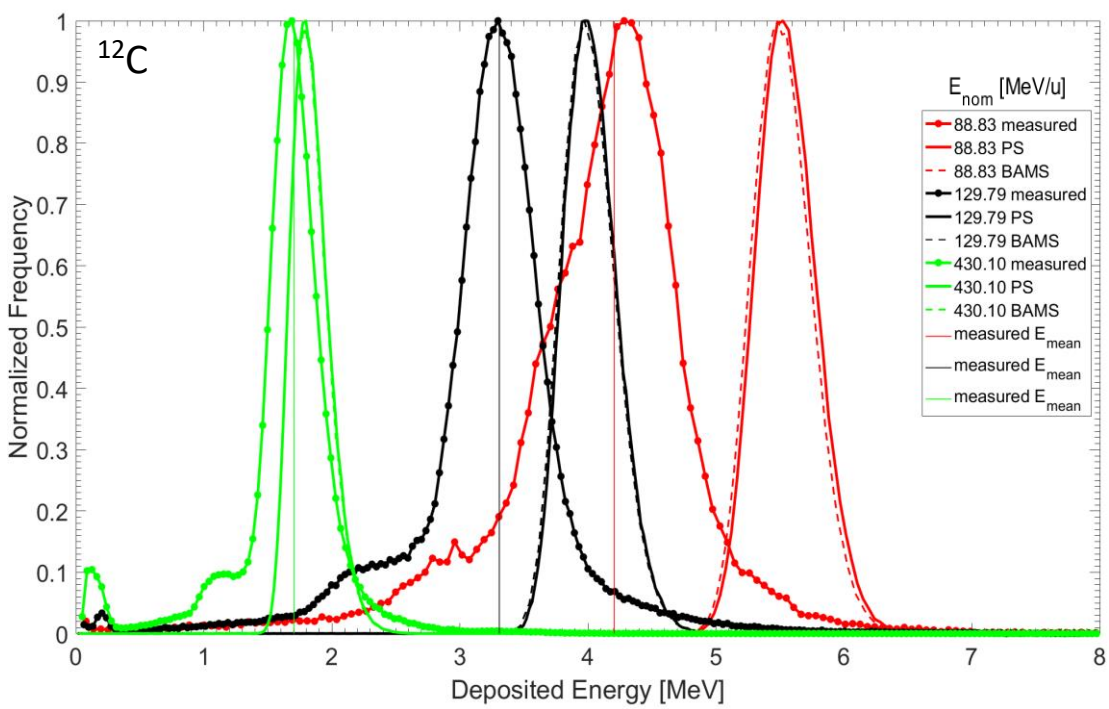

Figure 4.2.3. Measured (solid lines with markers) and simulated (solid and dashed lines) energy deposition distributions for ^{12}C ions of three different primary beam energies in a 100 µm thick silicon sensor. For the simulation of the ion beam phase space files (PS) or corresponding to the water equivalent thickness of the BAMS were used. Vertical lines show the location of the measured mean deposited energy. Each histogram was normalized to its maximum.

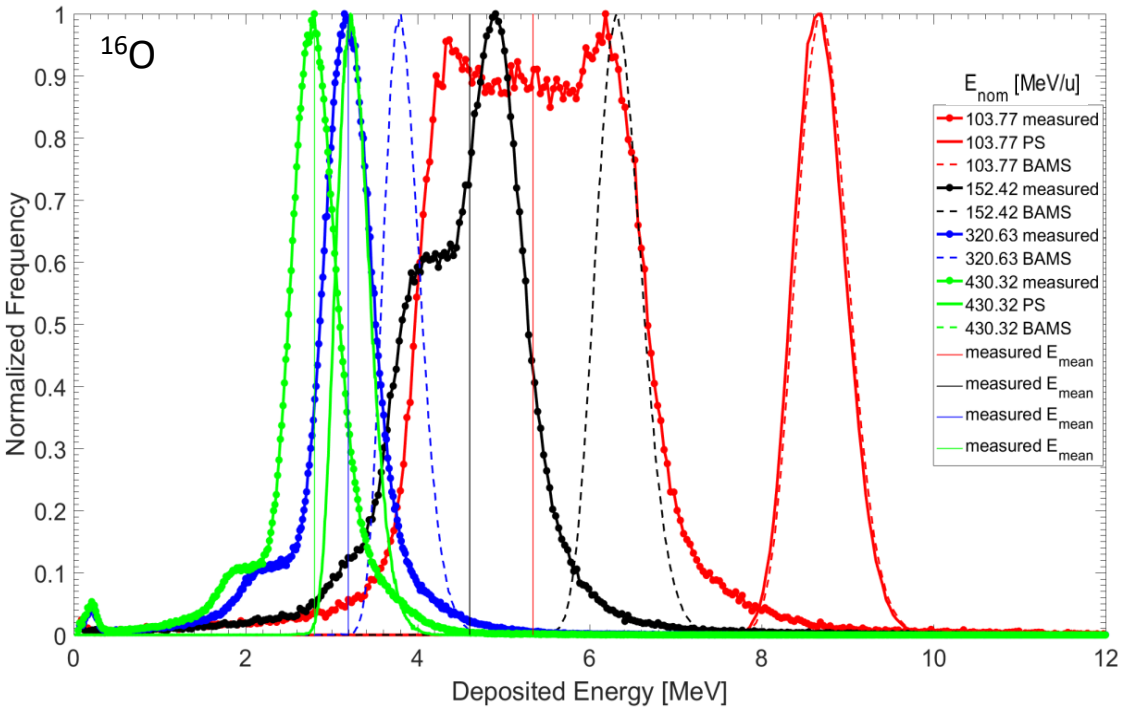

Figure 4.2.4. Measured (solid lines with markers) and simulated (solid and dashed lines) energy deposition distributions for ^{16}O ions of four different primary beam energies in a 100 µm thick silicon sensor. For the simulation of the ion beam phase space files (PS) or corresponding to the water equivalent thickness of the BAMS were used. Vertical lines show the location of the measured mean deposited energy. Each histogram was normalized to its maximum.

As expected, the obtained measured and simulated energy loss distribution in the silicon sensor showed a shape of Vavilov distribution with the so-called *Landau tail* in the region of high deposited energy. The Landau tail was more prominent in lighter ions exhibiting low deposited energies, i.e., in beams with higher primary beam energies like the energy step 255 in ^{1}H and ^{4}He ion beams. The observed skewed profiles changed into a Gaussian-like shape for ^{12}C and ^{16}O ions, mainly in the simulated spectrum of all the analyzed energy steps. As a consequence of the distribution of the deposited energy spectra, the mean deposited energies were located towards the Landau tail as displayed for the experimental results in Figures 4.2.1- 4.2.4. This situation was different for ions with low primary beam energy, for which the mean deposited energies were shifted towards the most probable deposited energy. This was because of the more Gaussian-like distributions.

The lower tails of ^{1}H and ^{4}He simulated spectra showed steeper fall-offs than those in the measured spectra, characteristic that was more evident in the spectrum of beams

with lower primary beam energies. The presence of knobbed lower tails (bulky regions in the zone of low deposited energy) was found in all the measured ion beams due to background and artifacts, nevertheless this characteristic was absent in the simulation´s results.

It was also noticed that the energy loss spectra obtained with the Monte Carlo simulations were consistently narrower when compared to the results of the experiments for all the studied primary beam energies and ion types. The highest difference, already perceptible by eye, was found for ^{12}C and ^{16}O ions with the lowest primary beam energy (energy step 1, depicted by the red curves in Figures 4.2.3 and 4.2.4). With regard to the ^{16}O spectrum with this energy, large fluctuations in the measured signal were observed between 4 and 7 MeV. Moreover, a convexity of the spectrum in this energy region was not reached but rather a concave shape was found, behavior exhibited only in this particular case. This effect was due to fact that for high energy depositions the Timepix device is out of the region where it is correctly working.

Concerning the implemented approaches for the simulation of the beam, it was found that both lead to very similar energy loss spectra with regard to its shape and width. For ^{16}O ions with primary beam energies 152.42 MeV/u and 320.63 MeV/u (energy steps 21 and 125, respectively) the phase space files were not available, hence the Monte Carlo simulations were performed using only the BAMS approach.

As stated before, in the case of ^{12}C and ^{16}O ion beams large differences can be seen between the experimental and simulated energy loss spectra with regard to the shape and the location of the most probable deposited energy. All the simulations presented the most probable energy loss in higher energies when compared to the measured spectra, although this difference tended to get smaller as the primary beam energy of the ions got higher, i.e., for lower energy depositions.

4.2.2 Mean deposited energy and width of the deposited energy spectra

From the energy deposition spectra of measured and simulated data, two quantities were of interest for this work: the mean energy deposited and the width of each spectrum. For the computation of both quantities, only energy deposition bins with at

least 15% probability (with respect to the maximum) were used to avoid the negative influence of the signal artifacts of the spectrum, present in low deposited energies.

Since the data was grouped in bins to generate the histograms, the mean energy deposited was calculated according to:

$$\overline{E} = \frac{\sum x_i f_i}{\sum f_i} \tag{4.1}$$

where f_i is the corresponding frequency of bin x_i .

For the calculation of the FWHM, each spectrum was divided in two parts: a first half containing data with increasing frequencies (from 0 to 1), and a second half containing data with decreasing frequencies (from 0.99 to 0). After this, two points near the frequency equal to 0.5 were chosen in each half: in the first half one point was the last point with frequency smaller than 0.5 and the other point was the first point with frequency higher than 0.5. Conversely in the second half, one of the points was the last point with frequency higher than 0.5 and the other was the first point with frequency smaller than 0.5. Once these points were found, a linear interpolation between them was conducted in each half to obtain the bins with frequency equal to 0.5 following the formula:

$$x = \frac{(y - y_1)}{(y_2 - y_1)}(x_2 - x_1) + x_1 \tag{4.2}$$

where

x_1 is the bin with frequency y_1

x_2 is the bin with frequency y_2

x is the deposited energy with frequency $y = 0.5$

The previously explained procedure is illustrated in Figure 4.2.5 below.

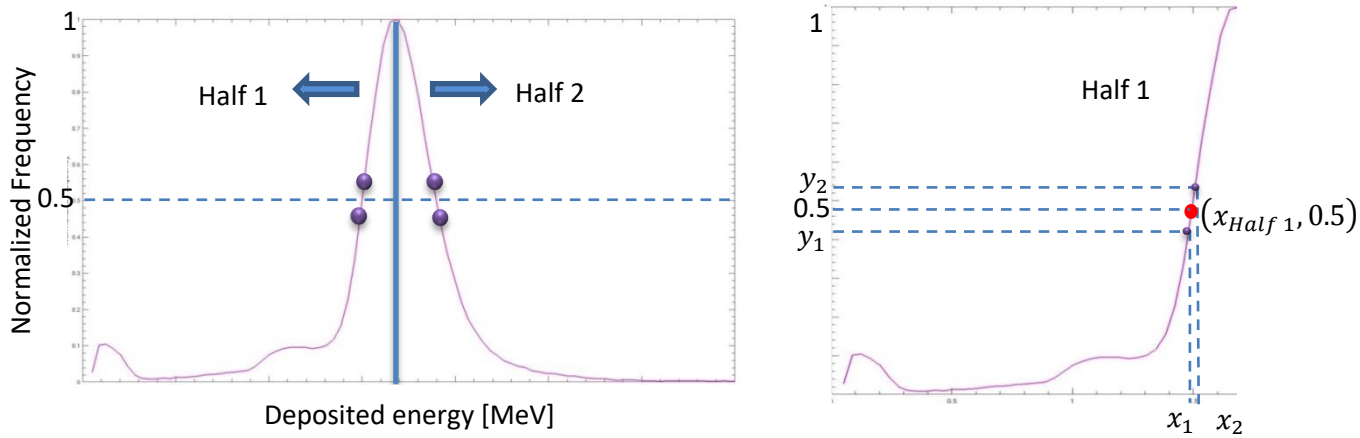

Figure 4.2.5. The division of the data in two halves based on the maximum and the two selected points (purple circles) below and above the frequency of 0.5, is depicted in the left panel. In the right panel, zooming in the first half (Half 1), the red point depicts the bin with the frequency equal to 0.5. The linear interpolation was made in order to find $x_{Half\ 1}$, between the points with coordinates (x_1, y_1) and (x_2, y_2).

When the bins $x_{Half\ 1}$ and $x_{Half\ 2}$ were obtained in each half (respectively), the FWHM was calculated by subtracting the values:

$$FWHM\ [MeV] = x_{Half\ 2} - x_{Half\ 1} \qquad (4.3)$$

For the formerly calculated quantities, the differences relative to the Monte Carlo simulations were computed using the formula:

$$relative\ difference\ [\%] = \frac{(x_{measured}[MeV] - x_{simulated}[MeV])}{x_{simulated}[MeV]} \times 100 \qquad (4.4)$$

where x can be either the calculated mean deposited energy or the calculated FWHM.

The correlation between simulated and measured values of the mean deposited energy and the FWHM will be presented in the next pages, including the corresponding relative differences.

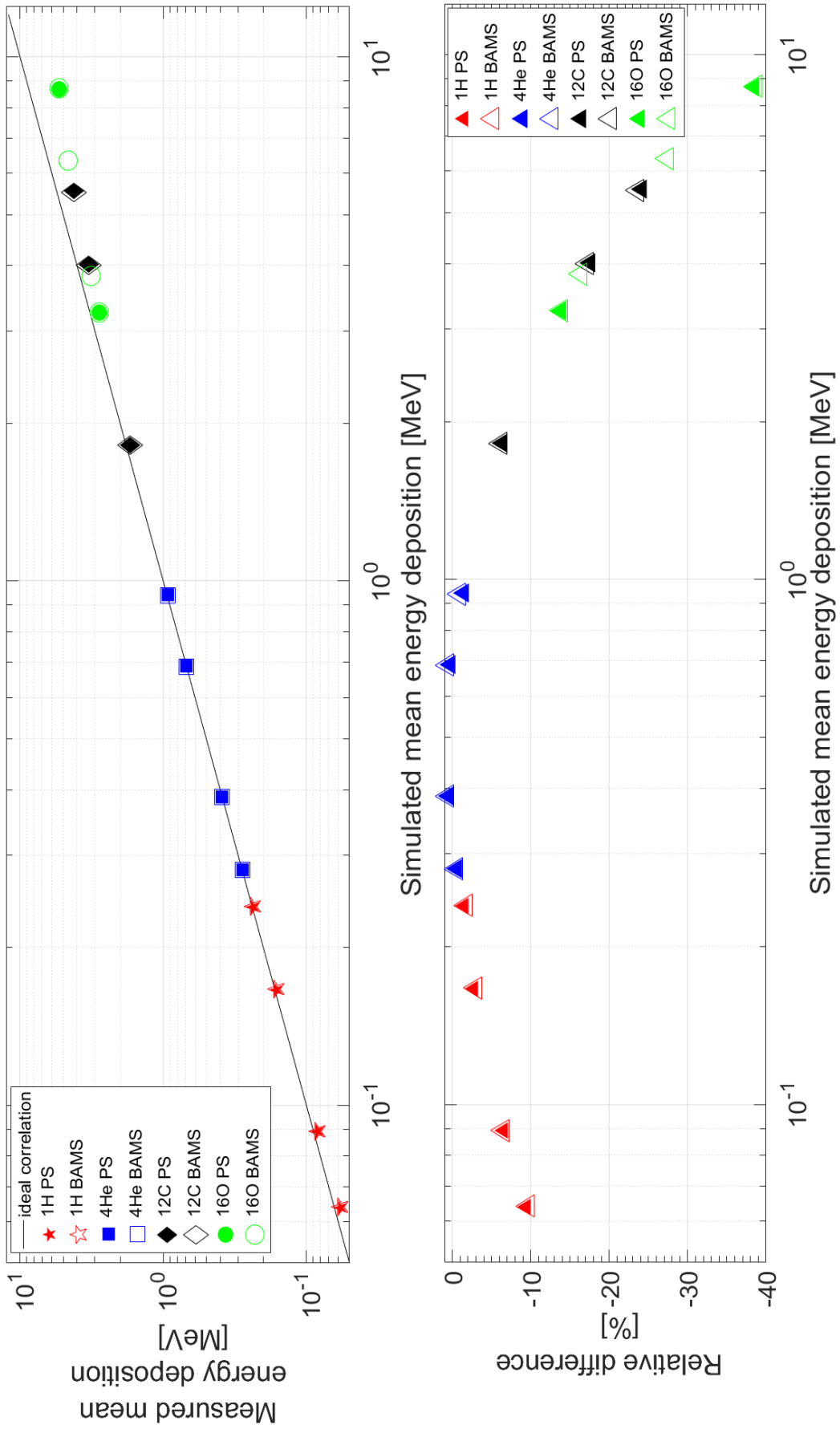

Figure 4.2.6. Upper panel: Correlation between simulated and measured mean energy deposited in a 100 µm thick silicon detector for ^{1}H, ^{4}He, ^{12}C and ^{16}O ions. Filled markers represent simulations with phase space files whereas empty markers represent simulations with BAMS. The black line shows the ideal one-to-one correlation between measured and simulated means. In the lower panel the relative differences between simulated and measured mean Energy deposited is shown.

In the preceding graph, the points are located in the following order for the four ion species (from left to right in the x axis): first the point which corresponds to the highest initial energy (step 255 or 205 in the case of ^{16}O ions), then the points of intermediate initial energies (steps 125 and 21, respectively) and finally the point with the lowest initial energy (step 1). The mean simulated energy deposited ranged from 0.0578 MeV to 8.707 MeV, equivalent to 0.578 MeV/mm and 87.07 MeV/mm for a 100 μm thick detector. Similarly, the mean measured energy deposited was between 0.64 MeV/mm and 53.41 MeV/mm. As has been illustrated in Figure 4.2.6, the implemented approaches for the simulation of the beam lead to very similar mean deposited energy values. The highest difference was of 33 keV for ^{12}C ions of initial energy 88.83 MeV/u.

For ^{1}H ions the measured mean energy deposited was closer to the simulated mean as the primary beam energy decreased, i.e., towards higher deposited energy values in Figure 4.2.6. The relative differences for this ion type ranged between 1.7% and 9.7%.

The measured mean energy deposited for ^{4}He ions was in a very good agreement with the simulated values for the four investigated primary beam energies (50.57 MeV/u up to 220.51 MeV/u), with relative differences between 0.6% and 1.4%.

It was found that the measured mean energies deposited by ^{12}C ions deviated from the simulated mean values in an increasing way towards the lowest primary beam energy. For 430.10 MeV/u (energy step 255) the relative difference was of 6.2%, while the subsequent energies deviated in 17.3% and 24.1% from the expected values. A similar situation was observed for ^{16}O ions, but in this case even the smallest relative difference (corresponding to the highest primary beam energy) was already of 13.9%, reaching deviations up to 38.6% for the lowest primary beam energy.

Limitations in the electronics to process high energy deposits produced by heavy ions compromised the linearity of the detector's response. This highly deteriorated the measurements with ^{12}C and ^{16}O ion beams. Furthermore, recombination effects taking place in the silicon sensor could have contributed to a lower collected charge, causing an underestimation of the mean deposited energy values.

Since it was observed that some of the points in Figure 4.2.6 deviated from the ideal line in a systematic way, interest arose in whether an additional calibration (valid for ions

only) can be found, which would correct for this behavior. A second degree polynomial was found to fit the points as displayed in Figure 4.2.7, especially in the region of higher deviations. The quality of the fit was evaluated by means of the statistic R-square with an achieved value of 0.9994. This value means that the fit explains 99.94% of the total variation in the data about the average. Using the fitted function as an additional calibration valid for ions, it was possible to reduce the relative difference between the simulations and experimental data significantly in the cases reported in Table 4.3:

Ion	Energy [MeV/u]	Relative difference before fit [%]	Relative difference with additional ion-calibration [%]
^{1}H	221.06	9.4	3.6
	142.66	6.5	0.8
^{12}C	430.10	6.2	4.3
	129.79	17.3	0.5
	88.83	24.1	2.8
^{16}O	430.32	13.9	1
	320.63	16.4	0.1
	152.42	27.4	3.9
	103.77	38.4	10

Table 4.3 The difference between experimental and simulated data after performing a second polynomial grade fit was reduced for ^{1}H, ^{12}C and ^{16}O ions of the primary beam energies investigated.

In the case of ^{1}H ions of energy step 21 and 1, as well as for the four energy steps of ^{4}He ions, the fit increased the relative differences.

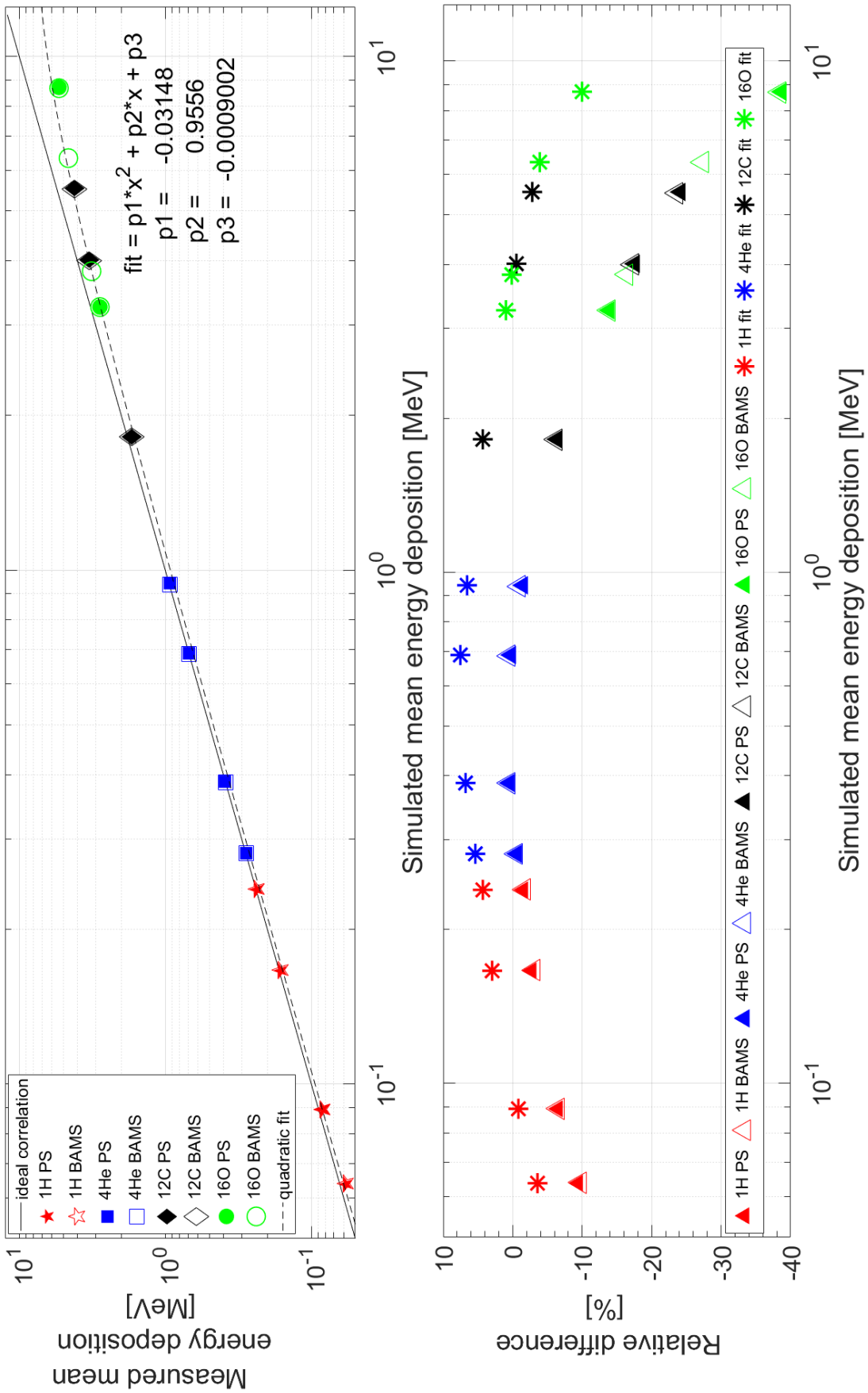

Figure 4.2.7. A second degree polynomial was found to fit the points presented in the previous plot. The residual differences between measured and simulated mean energy deposited are reduced when this fit is considered.

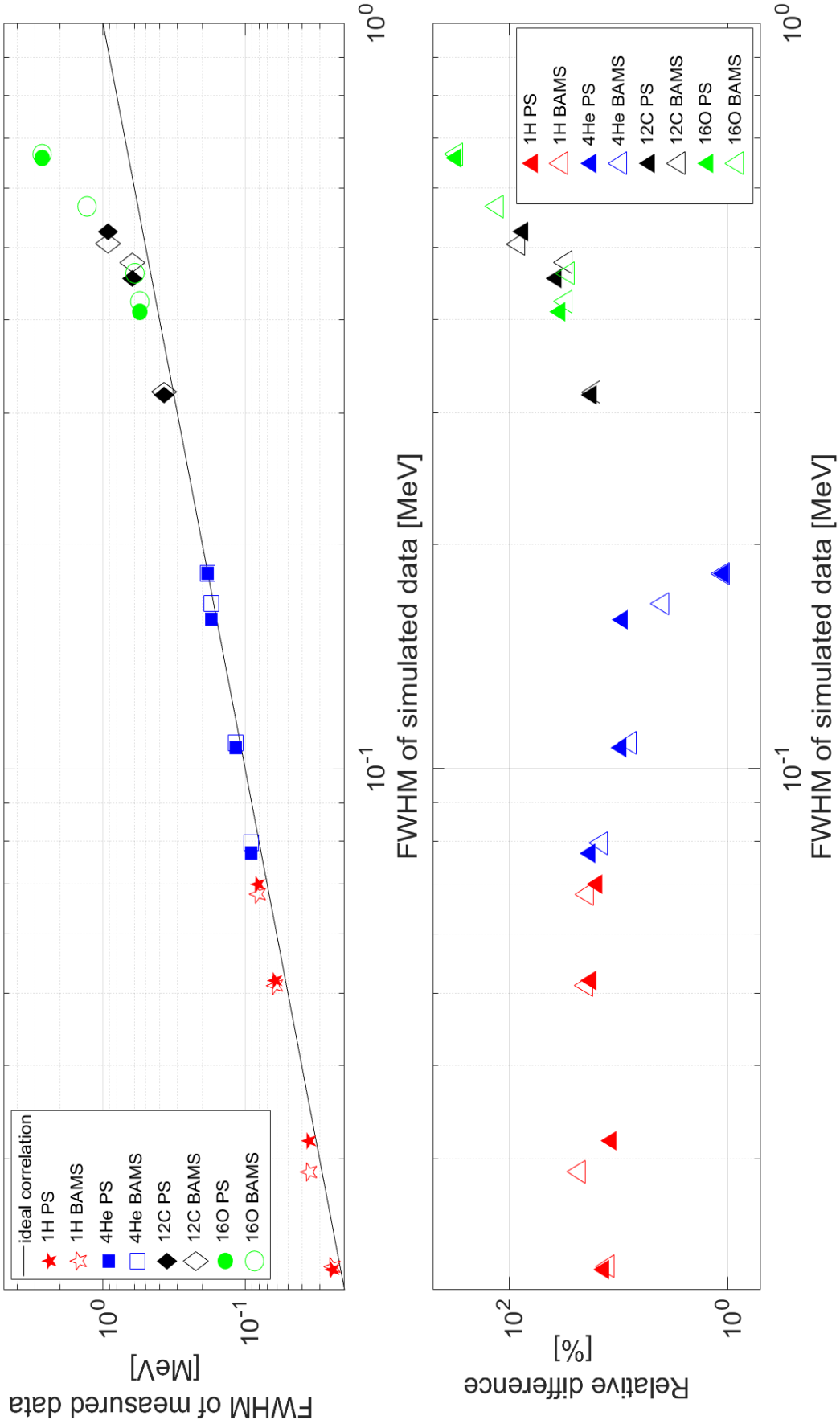

Figure 4.2.8. Correlation between simulated and measured width (FWHM) of energy deposition spectra for ^{1}H, ^{4}He, ^{12}C and ^{16}O ions. Filled markers represent simulations with phase space files whereas empty markers represent simulations with BAMS. The black line shows the ideal one-to-one correlation. In the lower panel the relative difference between the two FWHM values is shown.

The FWHMs of the measured energy loss spectra were in general larger than those obtained with the Monte Carlo simulations, as shown in Figures 4.2.1 - 4.2.4, for all the investigated ion species. In Figure 4.2.8, a plot displaying the correlation between experimental and expected width of the energy deposition spectra for all investigated ion types and primary beam energies is presented. The corresponding relative differences are included as well. In this Figure it is possible to distinguish that ^{12}C and ^{16}O ions exhibited the largest differences between measured and simulated width of the energy deposition spectra. These differences increased as the primary beam energy decreased. The relative difference between experiments and phase space simulations of the width of the energy deposited spectra for ^{1}H ions lied between 11.7% and 17.9%, while for ^{4}He ions the differences ranged between 1.1% and 18.2%. The corresponding values for ^{12}C ions were 17.7% and 75%. For ^{16}O ions the relative difference varied between 29.02% and 306.3%. In particular, the large relative differences obtained for ^{16}O ions with the two lowest beam energies arose from the significantly deteriorated measured spectra.

4.2.3 Comparison between two different sensitive layer thicknesses: 100 µm vs. 300 µm thick Timepix sensors

In a previous work, Gehrke T. et al. [31] used a Timepix detector with a 300 µm thick silicon sensor to measure the energy deposition of single ^{1}H, ^{4}He and ^{12}C ions. In this investigation, the detector was operated in energy mode with the sensor fully and partially depleted. When the sensor was operated fully depleted, saturation effects due to the detected high signal were found. The observed saturation effects were then decreased changing the depletion zone of the sensor from 300 µm to 210 µm by lowering the bias voltage. Interest arose in making a comparison of the performance of the device used in [31] against the 100 µm sensor used in this work, particularly in the energy region for which saturation was observed. For the intended comparison, the cases of full and partial depletion of the 300 µm sensor were considered.

In the upcoming pages, the energy deposition spectra of ^{1}H, ^{4}He and ^{12}C ion beams in fully depleted 100 µm and 300 µm silicon sensors are presented (Figures 4.2.9 - 4.2.11). For full depletion, a bias voltage of 5 V (100 µm sensor) and 40 V (300 µm sensor) was

applied. In the following, the shown Monte Carlo simulations were conducted using the phase space files to simulate the ion beam.

^{1}H ions

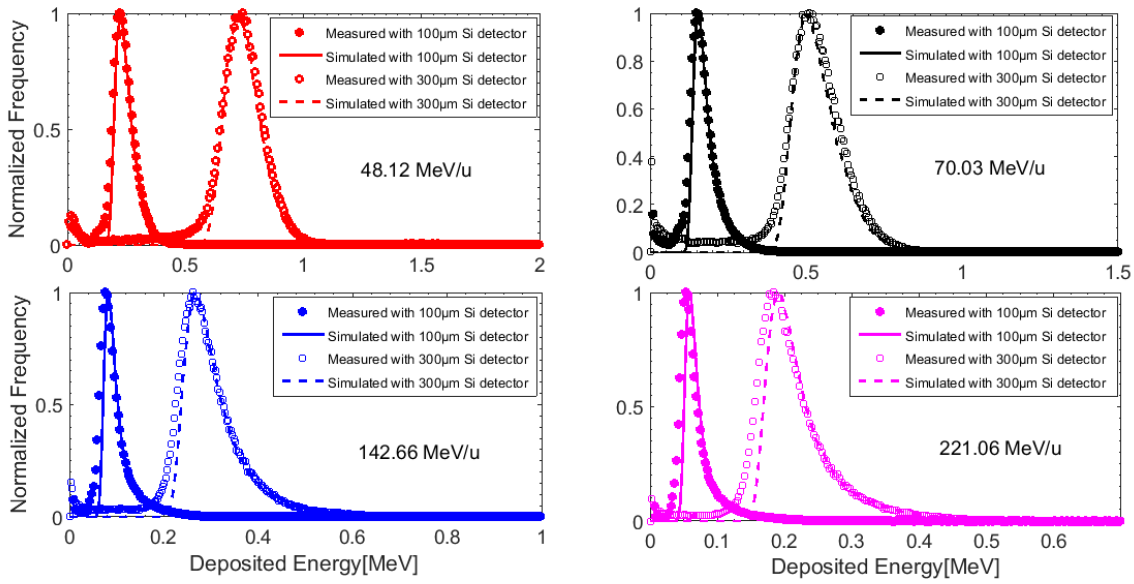

Figure 4.2.9. Measured and simulated energy deposition spectra for ^{1}H ions of four different primary beam energies. Full circles and solid lines are the results for a 100 μm thick detector (measurements and simulations, respectively) whereas empty circles and dotted lines belong to a 300 μm thick detector. Both detectors were used fully depleted. Data of 300 μm detector reprinted from [31].

^{4}He ions

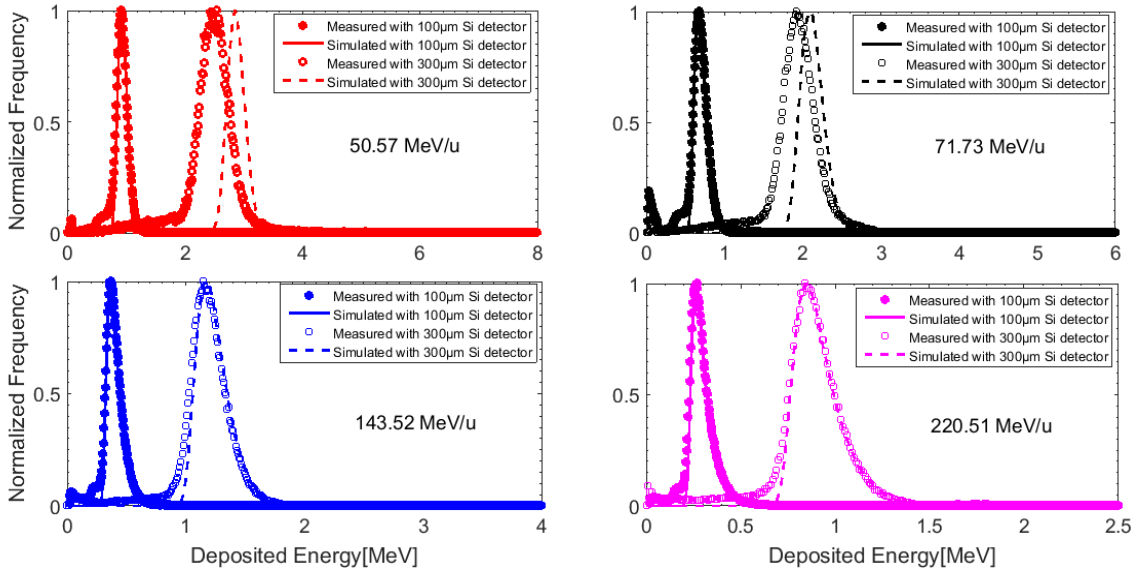

Figure 4.2.10. Measured and simulated energy deposition spectra for ^{4}He ions of four different primary beam energies. Full circles and solid lines are the results for a 100 μm thick detector (measurements and simulations, respectively) whereas empty circles and dotted lines belong to a 300 μm thick detector. Both detectors were used fully depleted. Data of 300 μm detector reprinted from [31].

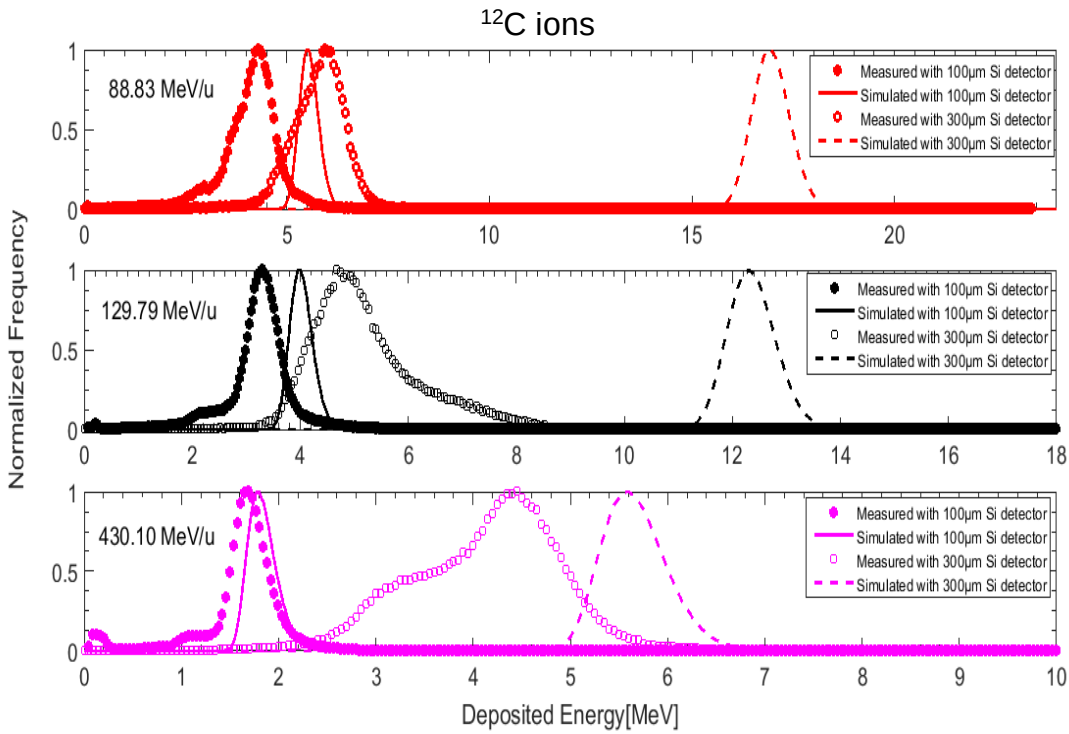

Figure 4.2.11. Measured and simulated energy deposition spectra for ^{12}C ions of three different primary beam energies. Full circles and solid lines are the results for a 100 μm thick detector (measurements and simulations, respectively) whereas empty circles and dotted lines belong to a 300 μm thick detector. Both detectors were used fully depleted. Data of 300 μm detector reprinted from [31].

In both detectors, the experimental results for ^{1}H ions were found to be in good agreement with the Monte Carlo simulations with regard to the shape and the width of the energy deposited spectra. The lower tail of the measured deposited energy distributions for both detectors tended to have gentler fall-offs than those of the simulated results.

While for ^{4}He ions the thinner detector behaved almost ideally for the four investigated initial energies, the most probable energy deposited measured with the thicker detector started to exhibit a shift towards lower energies. The largest shift was found in the lowest primary beam energy and it had a tendency to get smaller with higher initial energy, to the point where simulations and measurements were in agreement.

For ^{12}C ions, both detectors showed differences in shape and width of the spectra in comparison with the simulated data sets. The differences were smaller for higher primary beam energies, but no satisfactory agreement between measurements and simulations was found. The found differences were always larger for the 300 μm thick sensor.

With the intention of comparing the mean deposited energies in both sensors, the measured values were divided by the sensor thickness in millimeters, i.e. by 0.1 mm in the case of the 100 µm thick sensor and by 0.3 mm in the case of the 300 µm thick sensor. The corresponding correlation plot may be found in Figure 4.2.12. The thicker sensor was found to be more reliable for ^{1}H ions, since the maximum observed difference was of 4.3%, in comparison to the 9.4% achieved with the thinner sensor. For ^{4}He and ^{12}C ions instead, the 100 µm device showed smaller relative differences. The maximum observed difference for ^{4}He ions with the 100 µm detector was of 1.4%, while the corresponding value achieved with the 300 µm device was of 12.9%. For ^{12}C ions, the maximum found differences for the 100 µm and the 300 µm sensors were 24.1% and 65.6%, respectively.

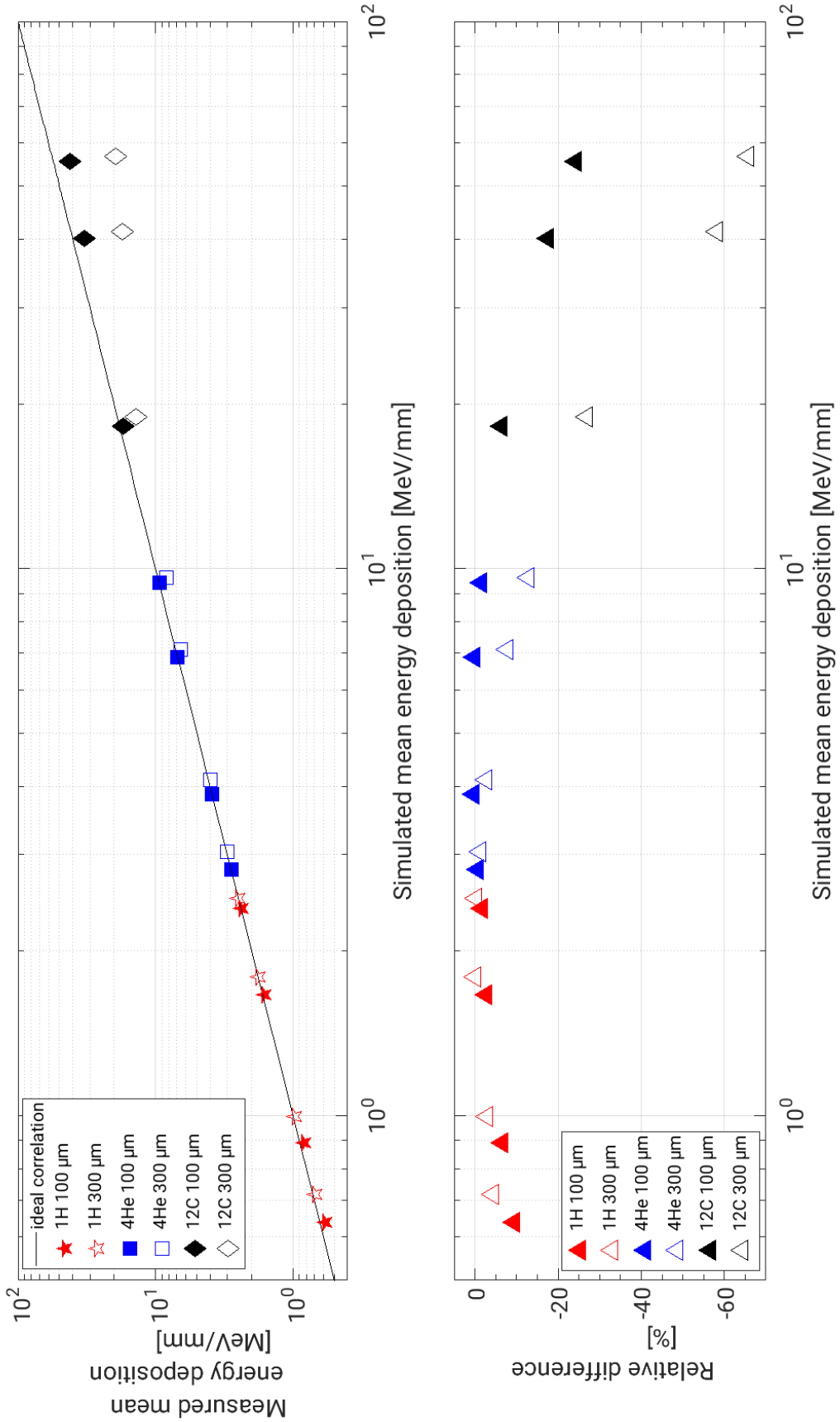

Figure 4.2.12. Upper panel: correlation between measured and simulated mean energy deposited per millimeter in 100 µm and in 300 µm thick silicon sensors for ^{1}H, ^{4}He and ^{12}C ions. In both cases the detectors were operated fully depleted. Filled markers represent points for the 100 µm detector while empty markers belong to the 300 µm detector. The black line shows the ideal one-to-one correlation. Lower panel: the relative differences between the two mean values is shown.

The results of measurements and Monte Carlo simulations of primary ion energy deposition in a partially depleted 300 µm silicon sensor from [31] are now compared with the obtained results with a fully depleted 100 µm silicon sensor. The corresponding spectra for ^{1}H, ^{4}He and ^{12}C ion beams are presented in Figures 4.2.13 - 4.2.15.

To fully deplete the 100 µm sensor, a bias voltage of 5V was applied. Instead, a bias voltage of 10 V was applied to the 300 µm sensor in order to obtain a depletion thickness of 210 µm. In this new scenario for the 300 µm sensor, the collected signal was performed in a smaller volume. Therefore, the signal to electronics was lower, reducing in this way the saturation effects. Like in the previous comparison, the correlation plot of mean deposited energy per millimeter (Figure 4.2.16) may be found in a forthcoming page. In the presented results, the ion beams were simulated using the phase space files.

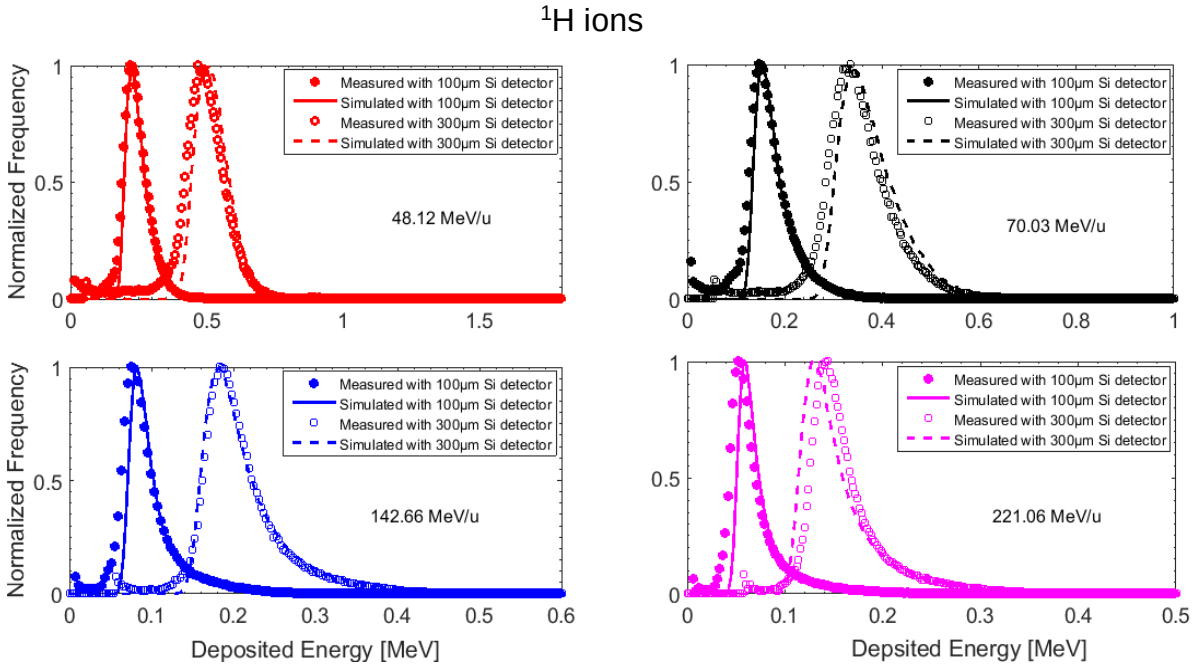

Figure 4.2.13. Measured and simulated energy deposition spectra for ^{1}H ions of four different primary beam energies. Full circles and solid lines are the results for a 100 µm thick detector (measurements and simulations, respectively) whereas empty circles and dotted lines belong to a 300 µm thick detector. The 300 µm detector was used partially depleted. Data of 300 µm detector reprinted from [31].

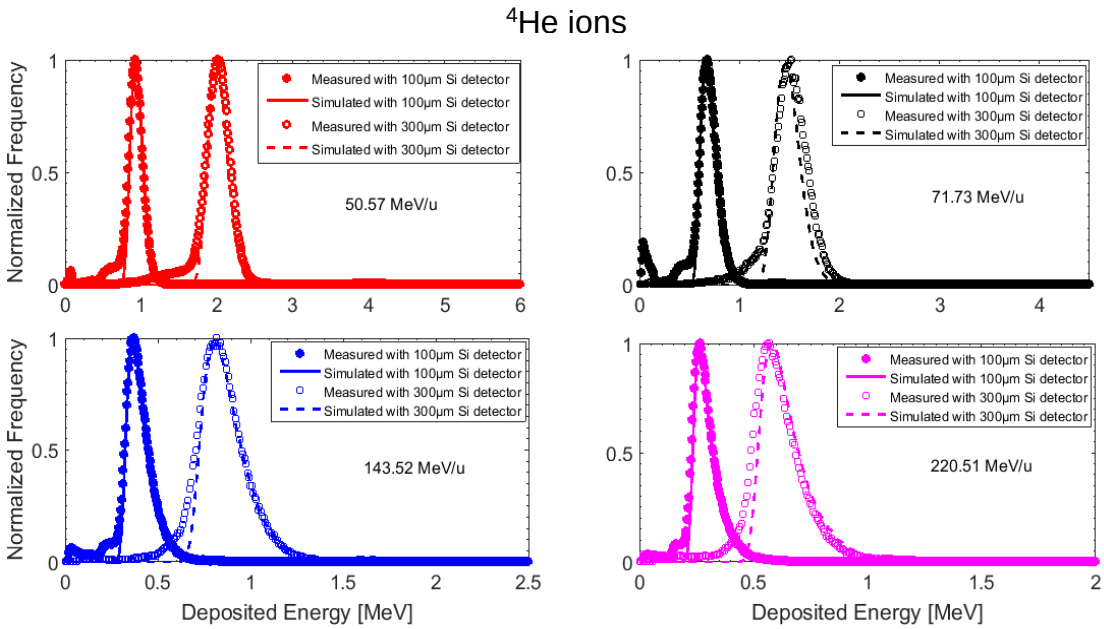

Figure 4.2.14 Measured and simulated energy deposition spectra for ^{4}He ions of four different primary beam energies. Full circles and solid lines are the results for a 100 μm thick detector (measurements and simulations, respectively) whereas empty circles and dotted lines belong to a 300 μm thick detector. The 300 μm detector was used partially depleted. Data of 300 μm detector reprinted from [31].

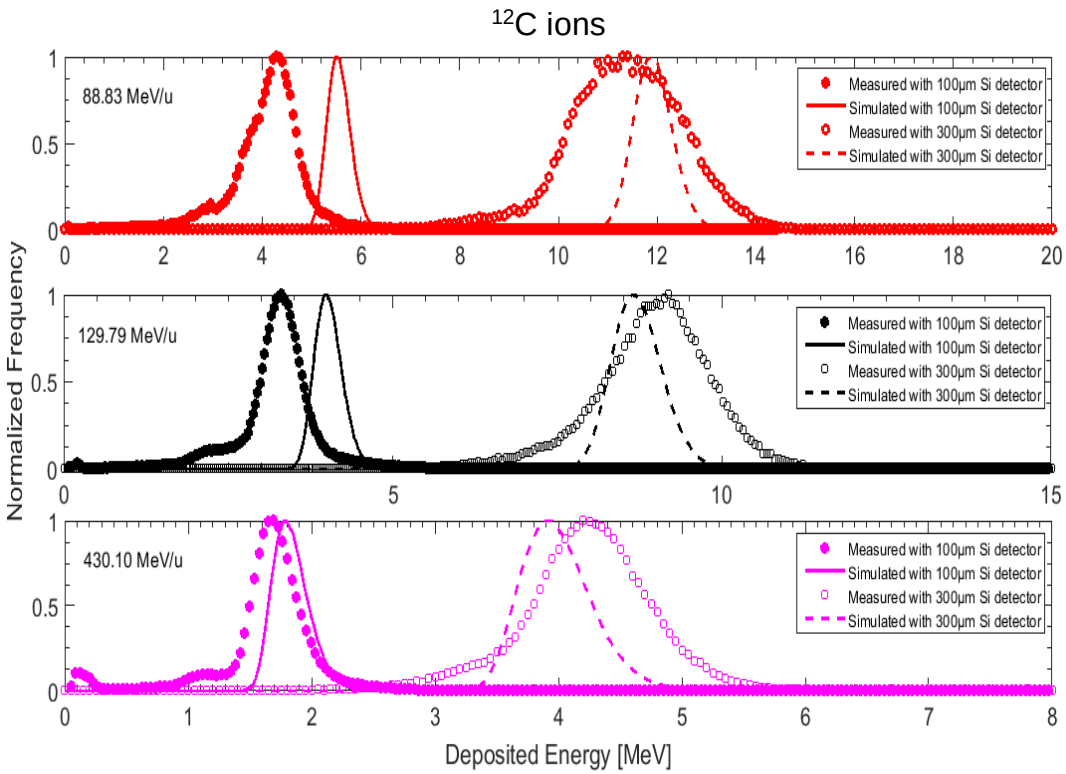

Figure 4.2.15 Measured and simulated energy deposition spectra for ^{12}C ions of three different primary beam energies. Full circles and solid lines are the results for a 100 μm thick detector (measurements and simulations, respectively) whereas empty circles and dotted lines belong to a 300 μm thick detector. The 300 μm detector was used partially depleted. Data of 300 μm detector reprinted from [31].

As shown in previous plots in Figures 4.2.13 – 4.2.15, the differences relative to Monte Carlo simulations in the location of the most probable energy deposited were reduced when the 300 µm detector was operated partially depleted. The partial depletion had a major impact in measurements with ^{4}He and ^{12}C ions in comparison to the fully depleted. However, for ^{1}H ions the relative differences were larger than when the detector was operated fully depleted. The reduction of relative differences between measurements and simulations was anticipated for ^{4}He and ^{12}C ions, since the signal collected in a smaller volume was lower than the signal collected in the whole sensor. Hence, a reduction in the readout chip electronics saturation was accomplished. No significant changes in the FWHM of the spectra were perceptible for any of the investigated ion types.

The correlation between simulated and measured mean deposited energy per millimeter for the 100 µm sensor (fully depleted) and the 300 µm sensor (partially depleted), is presented as a plot in Figure 4.2.16. Relative differences of mean deposited energy values (measurements with respect to Monte Carlo simulations) are included as well.

With regard to ^{1}H ion beams, the relative differences for the two highest mean energy deposits were smaller with the 100 µm sensor. Conversely, for the two lowest mean energy deposits the relative differences were smaller with the 300 µm sensor. The maximum observed deviation of the measured mean deposited energy with respect to its corresponding simulated value, was for the highest initial beam energy. It was of 9.4% with the 100 µm sensor in comparison with a 5.1% with the 300 µm sensor.

Concerning ^{4}He ion beams, the 100 µm presented smaller relative differences. The maximum relative difference was of 0.6% with the 100 µm sensor vs. 4.9% achieved with the 300 µm sensor.

In comparison to the results when both sensors were operated fully depleted, a very different situation was obtained for ^{12}C ions. Interestingly enough, measurements with the partially depleted 300 µm thick sensitive layer exhibited smaller relative differences in two of the three measured primary beam energies. For the highest mean deposited energy, the differences were 4.3% (with the 300 µm sensor) vs. 24.1% (with the 100 µm sensor). For the intermediate mean deposited energy value, the corresponding

deviations were 3.2% vs. 17.5%. Finally, for the lowest mean deposited energy similar relative differences were observed with both sensors.

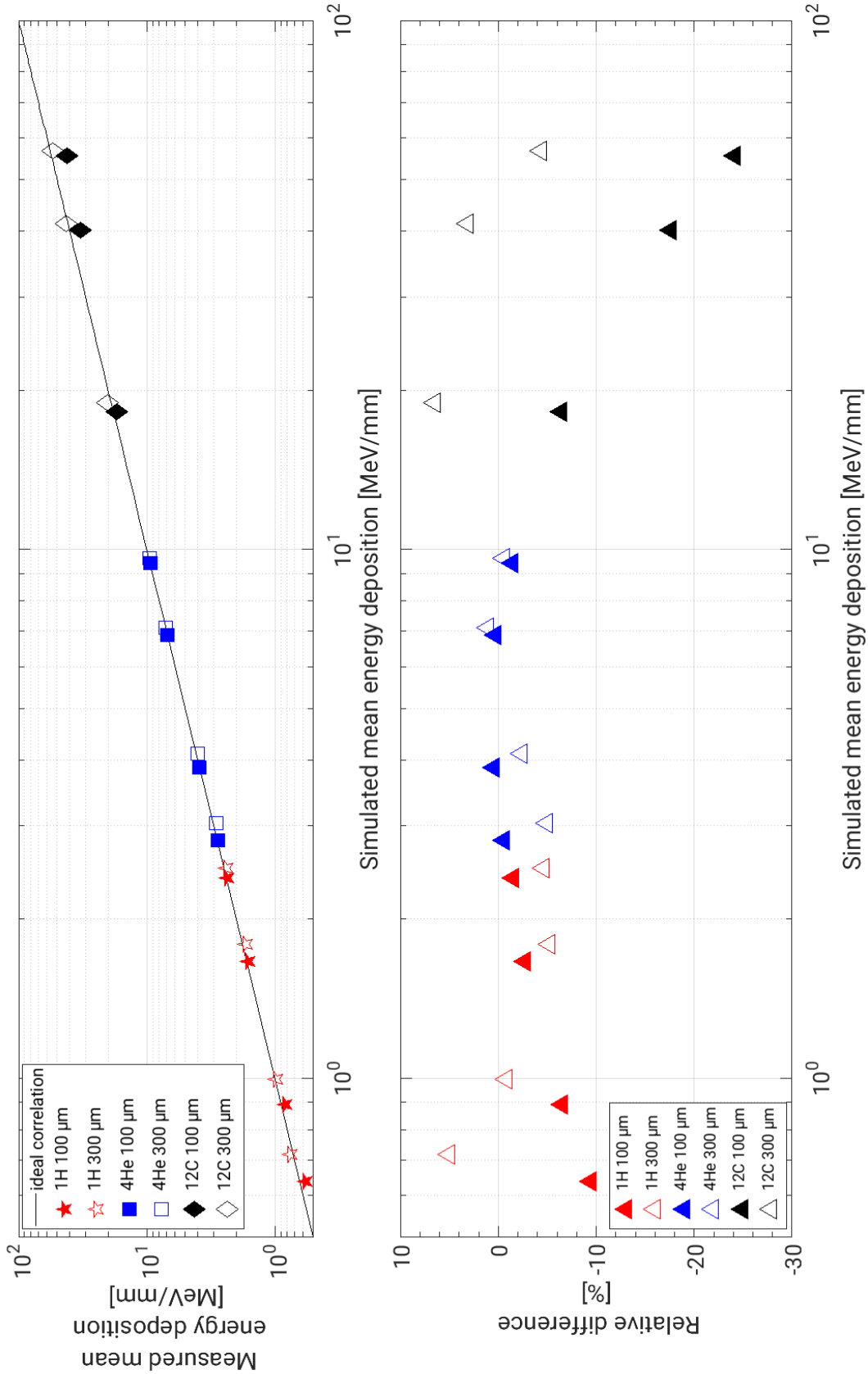

Figure 4.2.16. Upper panel: correlation between measured and simulated mean energy deposited per millimeter in 100 µm and in 300 µm thick silicon sensors for ^{1}H, ^{4}He and ^{12}C ions. This time the 300 µm detector was operated partially depleted, with a depletion thickness of 210 µm. Filled markers represent points for the 100 µm sensor while empty markers belong to the 300 µm detector. The black line shows the ideal one-to-one correlation. Lower panel: the relative differences between the two mean deposited energy values is shown.

"A thinker sees his own actions as experiments and questions, as attempts to find out something. Success and failure are for him answers above all."
Friedrich Nietzsche

5 Discussion and Outlook

This chapter aims to give an explanation of the results obtained with the 100 μm thick Timepix detector, presented in Chapter 4. With the intention of facilitating the reading and understanding, the structure followed in Results chapter has been maintained. A comparison of the performance of a 100 μm thick and a 300 μm thick Timepix detectors is included in this section, too. In addition, an outlook for possible improvements may be found.

5.1 Experimental Results

A significantly below the lowest therapeutically used fluence rate of ions was used during the conduction of the experiments in order to have sparsely distributed signals in space. This allowed avoiding the *pile-up effect* [37] that essentially consists in the artificial increase of the amplitude of a pulse due to the addition of signals coming from different particles hitting the same pixel.

5.1.1 The raw data

The observed two-peak pattern in the cluster size and in the energy deposition histograms (Figures 4.1.1 - 4.1.4) can be understood as will be described below.

The first peak (from left to right on the cluster size/energy deposited axis) is produced due to any of the following circumstances:

- When an ion arrives to the sensitive layer of the detector just before the acquisition frame has started, and thus the signal produced by such ion gets cropped by the beginning of the frame.
- When electrons, photons or ions with smaller atomic number Z than the primary ions impinge the sensor.
- When single pixels are malfunctioning.
- When a signal overshoot [38] is produced in a pixel.

In the first situation, the detected cluster will be small as long as the central part of the cluster is still above the threshold but the signal in the rim (see Nomenclature for the definition of *rim*) is already below it when the frame has started. Thus, in this scenario the rim will not be part of the cluster. The second situation is explained by the fact that clusters are formed due to the charge-sharing effect [39] which is dependent (among others) on the deposited energy of the particle traversing the sensitive layer of the detector. Hence, low-energy photons and electrons are expected to produce small clusters. For ions, as the primary beam energy is higher the energy deposition is lower, therefore clusters are smaller. Finally, the overshoot [38] effect is a detector artifact that arises when signals equal to or higher than 1 MeV are detected in the central pixel of a cluster, producing an oscillation in the read-out preamplifier. The oscillation leads to a fluctuating signal that is over and below the predefined threshold from time to time. As high signals (≥ 1 MeV) coming over the threshold are located in the center of the clusters, the overshoot will produce fake clusters that are rather small. The second peak observed in the histograms was produced by primary ions (charged nuclei of certain element, in this work either ^{1}H, ^{4}He, ^{12}C or ^{16}O) impinging the sensitive layer. Since primary ions are the particles with the highest atomic number Z interacting with the sensor, the highest possible energy loss will be by them. This means that their charge cloud would be bigger than the charge clouds produced by any other particle.

The two-peak pattern was more visible in the histograms of ^{12}C and ^{16}O ion beams in comparison with ^{1}H and ^{4}He beams. This is because they are more likely to produce overshoots in the read-out chip (due to the high energy loses) and also because of the variety of secondary ions that could be produced during their passage through the BAMS, or even within the sensor. The mentioned pattern was not visible in the

measurements with ^{1}H beams since for all the studied primary beam energies the overshoot effect was almost negligible. Also, electrons and photons can be still in the same peak as ^{1}H ions.

If the first energy step is considered for all the measured ions, clusters produced by a ^{1}H beam will be smaller than those produced by a ^{4}He beam, which in turn will be smaller than clusters of a ^{12}C beam and in the same way, they will be smaller than the ones created by an ^{16}O beam. As was experimentally confirmed, the higher Z the higher the energy loss, hence denser charge clouds that will expand and diffuse in the sensitive layer before being collected (under the influence of the same bias voltage) were created. Consequently, clusters were made up of more pixels and they were larger.

If the ion type is fixed instead, it was observed that the cluster sizes decreased as the primary beam energy increased. This is because even though particles with the same Z are traversing the sensor material, more energetic beams are composed of particles with higher momentum. Consequently, those particles spend less time crossing the detector having less time to interact with electrons. This means that less energy would be deposited in the sensitive layer and the created charge cloud would be smaller.

A similar situation prevails in the histograms of deposited energy. The first peak from left to right in the energy loss axis is related to the energy deposited in clusters that were cropped at the end or at the beginning of a frame, since they exhibit degraded volumes as a result of the lack of part of the signal. This peak can also be attributed to the overshoot clusters and to secondary particles reaching or created in the sensor.

5.1.2 Data post-processing

Concerning the percentage of rejected clusters by the cut in size, the high probability of overshoots occurrence during energy loss measurements of ^{12}C and ^{16}O ion beams explains why this post-processing step had a higher impact on the number of rejected clusters, compared to the percentage of rejection in ^{4}He and ^{1}H data. The high amount of rejected clusters was also related to the presence of secondary particles.

More overlapping clusters were present in the measurements with ^{12}C and ^{16}O beams because the size of the clusters produced by these particles was larger than that

produced by ^{4}He or ^{1}H ions. Hence, the chance of reaching neighboring pixels of other cluster(s) was higher. This can be further decreased in future work by lowering the beam intensity even more.

Of all ion species studied in this work, ^{1}H ion beams were the most susceptible to scatter during their travel in air towards the detector. The high occurrence of spatially cropped clusters is directly related to this fact. Consequently, the number of ions impinging the Timepix sensitive layer close to its border was higher than for the rest of the analyzed ions. Within the same ion type, the foci of the pencil beam in air is inversely proportional to its initial energy. So, the lower the primary beam energy the higher the impact of rejection of spatially cropped clusters.

5.2 Comparison of deposited energy in experimental data and simulations

5.2.1 Spectra of deposited energy in a 100 µm thick sensor

The observed highly asymmetric energy deposition spectra (Figures 4.2.1 and 4.2.2) with the so-called Landau tail extending towards the region of large energy loses is consistent with the Landau distribution that models the energy loss by ionization of charged particles in thin layers [40]. This distribution accurately describes the energy loss as long as the used detector can be considered as “thin” compared to the range of the particles traversing the sensitive material. The energy deposition distribution is expected to become a Gaussian distribution in the limit of many collisions (Central Limit Theorem) [41]. This was the case for ^{12}C and ^{16}O beams with the lowest primary beam energy, which are expected to experience many interactions within the sensor and therefore depositing a large amount of energy. The resultant energy loss spectra were less asymmetric as can be seen in Figures 4.2.3 and 4.2.4.

The mean energy deposition in the silicon sensor is larger for less energetic ion beams crossing the sensitive material because of the $1/\beta^2$ dependence of the energy-loss rate dE/dx (Equation 2.4): ions with smaller momentum spend more time traversing the sensor and hence more collisions might take place, increasing the amount of deposited energy in the sensitive material. This behavior is consistent with results depicted by red curves in Figures 4.2.1, 4.2.2, 4.2.3 and 4.2.4.

As the energy loss depends quadratically on the charge of the projectile, it was expected and confirmed by the Monte Carlo simulations and the experiments among the four utilized ion beams in this work, ^{16}O ions would exhibit the highest energy losses. ^{1}H ions instead, would be the ions depositing less energy in the sensitive layer of the Timepix detector.

As the Landau tail depends on the maximum transferrable energy T_{max} * which is dependent on β^2 , the beams with higher initial energies will exhibit a more pronounced Landau tail within the same ion type. Examples of this characteristic can be found in the measured spectra of energy step 255 ^{1}H and ^{4}He ion beams, depicted by green lines in Figure 4.2.1 and Figure 4.2.2.

The shape of the Landau distribution shifts the mean energy deposited from the most probable energy deposited towards higher values (T_{max}) due to its high asymmetry related to the infrequent high-energy-transfer collisions [42]. This behavior has been observed for the experimental data with vertical lines in Figures 4.2.1, 4.2.2, 4.2.3 and 4.2.4.

In the experimental results with ^{1}H and ^{4}He ion beams, low-energy deposits coming from detector artifacts were more frequent in the measurements when compared with the simulations. These deposits contributed to the gentle rising up of the spectra. In ^{12}C and ^{16}O ion beams it is possible that some fragments arising from the passage of the ions through the BAMS or generated in the detector are contributing to low energy deposits. They became visible like the bulging parts of the spectra.

5.2.2 Mean deposited energy and width of the deposited energy spectra

The good agreement between the two implemented approaches to simulate the ion beams shows the robustness of the Monte Carlo simulations. The obtained results were similar with regard to the shape of the deposited energy spectra, the width of the spectra (deviations up to 5.08%), the most probable deposited energy (deviations up to 0.74%),

* $T_{max} = \frac{2m_e c^2 \beta^2 \gamma^2}{1+2\gamma m_e I M+(m_e/M)^2}$ is the maximum kinetic energy transferred from a particle of mass M to an electron

and the mean deposited energy (deviations up to 0.60%). The maximum differences between simulations with the phase space files and simulations with the equivalent to the water thickness of the BAMS are reported in Table 5.1:

	Maximum difference		
Ion	**Width of the deposited energy spectra [MeV]**	**Most probable deposited energy [MeV]**	**Mean deposited energy [MeV]**
^{1}H	0.003	0.001	0.001
^{4}He	0.008	0.018	0.005
^{12}C	0.023	0.041	0.033
^{16}O	0.013	0.036	0.033

Table 5.1. Maximum differences between the phase space and the BAMS methods utilized for Monte Carlo simulations. Most of the maximum deviations (per ion type) were found for ion beams with the lowest initial energy.

The observed differences between experiments and simulations in the location of the most probable energy loss and the mean deposited energy of ^{12}C and ^{16}O ion beams can be attributed to the following causes:

- **Recombination effects** may take place in the sensitive layer of the Timepix detector during charge collection. As the energy loss in the sensor increases, ions interact more with the sensitive material creating more electron-hole pairs. Throughout their travel to the corresponding opposite polarity electrode to be collected, the likelihood of recombination increases. If recombination occurs, a loss in the pulse amplitude will be produced as a consequence. This phenomenon is also known as the plasma effect.
- At a certain value of collected charge per pixel called the distortion level (~ 1 MeV) [43], the electronics in the readout chip of Timepix may reach a saturation level. In turn, an artifact in which the central pixels of some clusters corresponding to high energy loss values might be overridden is produced [43]. This behavior has been observed in several studies using the Timepix detector. It has been called the **"volcano effect"** since the peak of the Gaussian-like clusters drops down resembling a crater, as showed in Figure 5.2.1 (a). Since the

above mentioned phenomenon is related to high energy deposits and high sensor bias voltage [43], it was expected that the differences between measurements and Monte Carlo simulations were smaller for higher primary beam energies. In those cases the deposited energy in the sensitive layer was smaller.

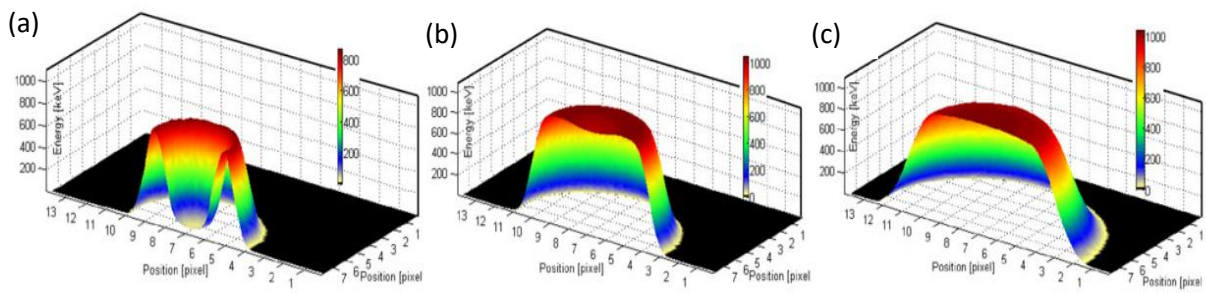

Figure 5.2.1 The volcano effect is dependent on the applied bias voltage. Here, 90 MeV ^{98}Zr ions were measured using a Timepix detector in TOT mode with an applied bias voltage of (a) 95 V, (b) 21 V and (c) 7 V. Reprinted from [43].

- It is also important to bear in mind that the Timepix detector has an energy resolution limit related to the predefined threshold. The threshold was equal to 5 keV for the assembly used in this work. This quantity means that if an impinging ion creates a cluster which originally would include pixels with a value equal or less than 5 keV, such pixels will not be taken into account. Therefore part of the deposited energy in the cluster would be lost, reducing the real deposited energy by that ion.

It has to be noticed that the Timepix device was originally designed as a photon counter and that in order to be operated in TOT mode it was calibrated using different gamma sources (i.e. emitted photons with known energies). Nevertheless, in this work protons and heavy ions have been utilized. This fact may also contribute to the large deviations from the expected spectra observed in the measurements with the heaviest ions (^{12}C and ^{16}O ion beams).

5.2.3 Comparison between two different sensitive layer thicknesses: 100 µm vs. 300 µm thick Timepix sensors

When both sensors were operated fully depleted, the 100 µm thick sensor showed smaller deviations from the expected mean deposited energy values at large ionization

densities (> 4 MeV/mm). The main reason is the lower signal produced in the sensitive layer, which the read out chip can process more reliably.

The detector used in this work had a more accurate performance for ^{4}He and ^{12}C ions, for which the 300 µm thick device exhibited saturation effects. The strong saturation effects (more than 10% deviation of the mean) in the 100 µm thick sensor were reached at a mean energy deposition of 32 MeV/mm, while for the 300 µm thick Timepix such saturation was observed for a mean energy deposition of 10 MeV/mm.

Experimental results measured with the 100 µm sensor were closer to Monte Carlo simulations with regard to the shape of the distributions and the location of the most probable deposited energy. Yet, for low energy deposits (observed in ^{1}H beams) measurements of mean deposited energy performed with the 300 µm sensor were more similar to simulations than measurements with a 100 µm thick sensitive layer. As results for mean deposited energies below 0.89 MeV/mm suggest, the 100 µm sensor is not sufficiently thick and thus the signal induced by radiation is low. In contrast, as more material to interact with is available in the 300 µm sensitive layer, more energy can be deposited in the sensor and the collected signal is higher. Therefore, when comparing the response to low energy deposits, higher scored signal lead to more accurate measurements.

Results of mean deposited energy measurements with both sensitive layers in terms of factors of improved or worsen detector performance are illustrated in Figure 5.2.2. In the context of this thesis, improvement means that measurements using the 100 µm sensor showed smaller deviations from Monte Carlo simulations than those obtained when measuring with the 300 µm thick sensitive layer. Worsening instead, means that the 100 µm sensor showed larger deviations from Monte Carlo simulations than the 300 µm sensor. As the relative difference obtained with the 300 µm sensor for ^{1}H ions of energy step 21 was practically zero, it was no possible to obtain the corresponding worsen performance factor.

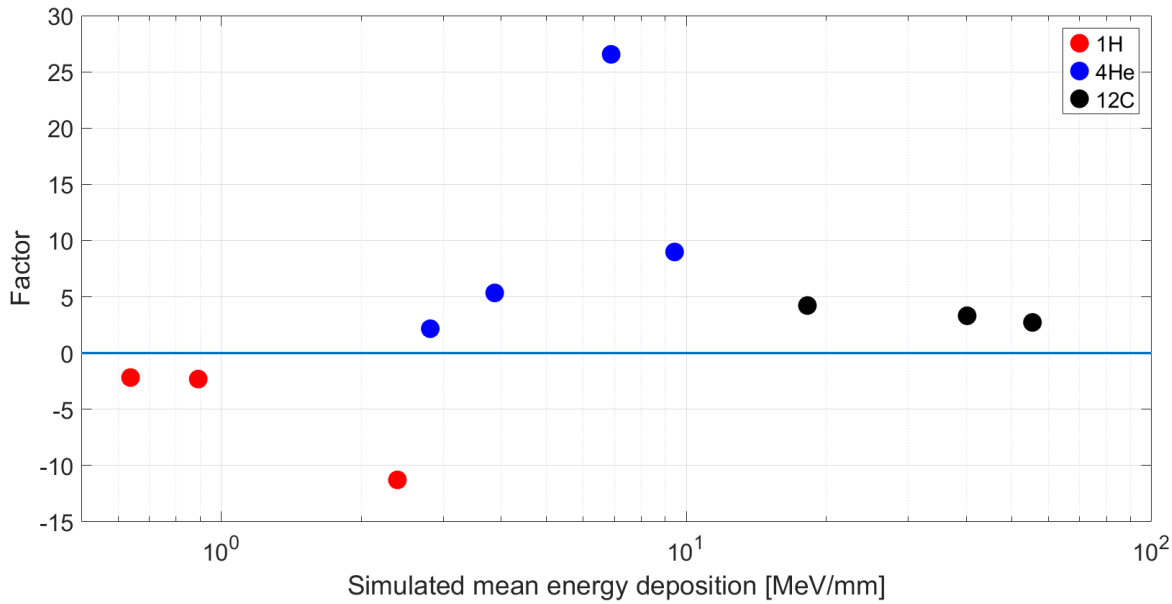

Figure 5.2.2 Factors showing an improved (above horizontal line) or a worsen (below horizontal line) detector performance when comparing measurements of mean deposited energy with a fully depleted 100 µm sensor vs. a fully depleted 300 µm sensor. Factors are shown for each primary beam energy and ion type analyzed in this work.

From the information depicted in Figure 5.2.2 it is possible to state that the relative difference obtained for ^{4}He ions depositing a mean energy of 2.813 MeV/mm in silicon (first blue point from left to right) with the 100 µm detector was two times smaller than the relative difference obtained with the 300 µm sensor. In other words, the difference between measured and simulated mean deposited energy with the 300 µm sensor was reduced to half its value when the 100 µm sensitive layer was used.

With regard to the measured mean deposited energy when operating partially depleted the 300 µm sensor, better detector performance was achieved when compared to the results with the 100 µm sensitive layer for ^{12}C ions. This indicates that a depletion thickness of 210 µm may represent a good compromise between the charge collection speed, the plasma effect, and electronics' capabilities related to high signals/linearity. For ^{4}He ions of energy steps 21, 125 and 255, the 100 µm sensor still performed better than the 300 µm one. Moreover, smaller differences relative to simulations were achieved for ^{1}H ions of energy steps 1 and 21. Figure 5.2.3 presents the factors of improved or worsen detector performance, in this new scenario:

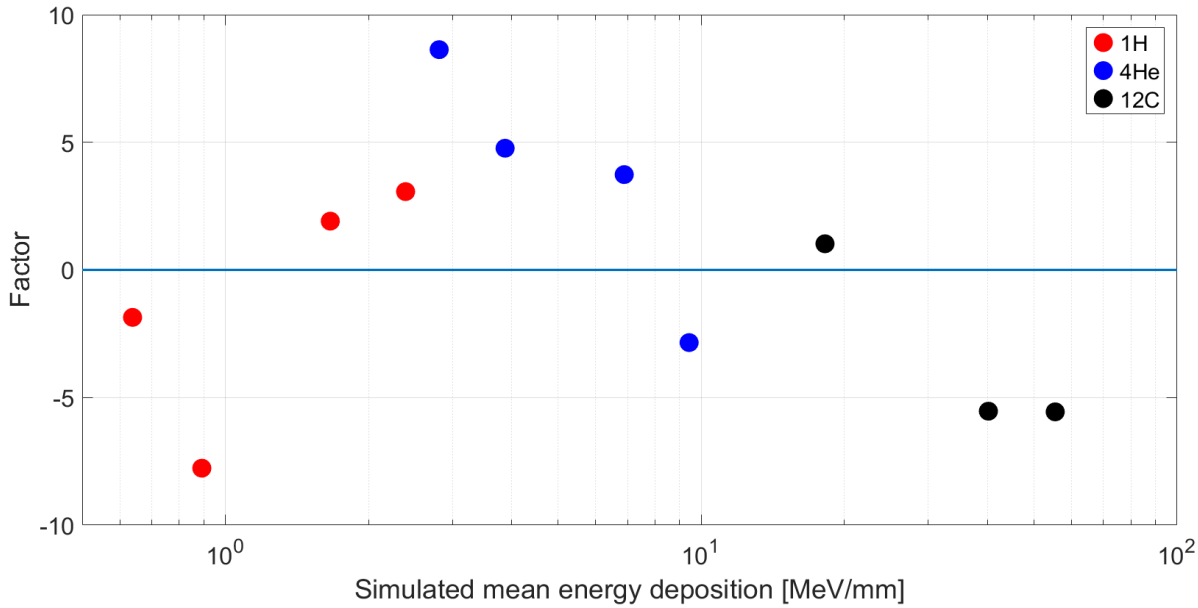

Figure 5.2.3 Factors showing an improved (above horizontal line) or a worsen (below horizontal line) detector performance when comparing measurements of mean deposited energy with a fully depleted 100 µm sensor vs. a partially depleted 300 µm sensor. Factors are shown for each primary beam energy and ion type analyzed in this work.

When looking at the calculated factor for ^{1}H ions of energy step 1, it can be stated that the difference between measured and simulated mean deposited energy per millimeter was three times smaller with the 100 µm sensor than with the 300 µm sensor. In contrast, two of the three measured primary beam energies of ^{12}C ions presented larger deviations from Monte Carlo simulations with the 100 µm sensor. The worst factor for this ion type was found for the beam with the lowest initial energy, and it was equal to 5.56. This is equivalent to 18% larger difference between measured and simulated mean deposited energy utilizing the 100 µm sensor.

5.3 Outlook

Applying a higher bias voltage could be useful to improve the 100 µm sensor performance when measuring high signals, e.g. with ^{12}C and ^{16}O ions. However, the increase in bias voltage should be done carefully to avoid sensor damage. Trying several depletion thicknesses between 100 and 250 µm with the 300 µm thick device would be useful to verify whether the ideal depletion thickness for measuring energy loss of heavy ion beams with a solid state Timepix detector is unique or not, and to find out the best compromise between acquisition times and artifacts reduction.

The successor version of the device used in this work, the Timepix3 detector, offers some advantages that could improve the accuracy of energy loss measurements especially with ^{12}C and ^{16}O ion beams namely [44]:

- Continuous readout [44], meaning it is dead time-free and hence much faster.
- Time resolution of 1.56 ns (vs. 10 μs) [44], therefore occurrence of overlaps is reduced and the use of higher intensities might be feasible.
- Possibility for readout of gas-filled detectors [44].
- The measurement of TOT vs. input charge must be monotonic for large positive charges (holes) up to 300 kh+ [45].

It is needed to experimentally test if Timepix3 is able to deal with the volcano effect observed in older versions. If so, Timepix3 would be a promising candidate to accurately measure large energy loses.

It would also be interesting to perform the experiments with a gas-filled sensor, especially for high energy deposits. The aim would be to test if the volcano effect can be reduced, since a lower density sensor material would be used.

Future experiments could include measuring energy deposition implementing a phantom set up. This would allow testing the detector capabilities in non monoenergetic - non single ion fields, mimicking more realistic clinical conditions.

In ion beam RT, the Bragg peak is positioned at the tumor's depth to achieve the maximum dose deposition at this volume. Moreover, LET increases along the Bragg peak. However, the ion beams used in this study had relatively high energies while the sensor thickness was just of 100 μm. Consequently, the range of measured deposited energy does not cover all possible LET values along the entire Bragg peak for heavy ions in silicon. Thus, further studies investigating the response of the Timepix detector to these high LET have to be carried out in the future.

"Life is an unfoldment, and the further we travel the more truth we can comprehend. To understand the things that are at our door is the best preparation for understanding those that lie beyond."
Hypatia

6 Conclusion

Energy deposition measurements are of great importance in different fields, mainly for radioprotection purposes and planning of radiotherapy treatments. In particular, measuring energy deposition by ions can bring benefits in areas such as Space Science and Medical Physics, in which people are exposed to ionizing radiation.

In the present work, monoenergetic ion beams of ^{1}H, ^{4}He, ^{12}C and ^{16}O ions with 3-4 energies each in the therapeutic range were used to evaluate the capability of a silicon pixelated detector Timepix with 100 μm thick sensitive layer to measure energy loss. For that purpose, a phantom-free set up was implemented and the detector was operated with full depletion of the sensitive layer using an applied bias voltage of 5V. The measurements were conducted at the Heidelberg Ion Beam Therapy center in Germany and the experimental results were compared with Monte Carlo simulations using the FLUKA code.

It was found that in the range of mean deposited energy between 0.638 MeV/mm and 18.196 MeV/mm in silicon, the Timepix detector has great potential to accurately measure energy loss since the experimental results exhibited deviations below 10% from the simulated expected values. In particular, for mean deposited energies between 2.813 MeV/mm and 9.428 MeV/mm, corresponding to ^{4}He ion beams with energies between 202.411 MeV and 882.613 MeV, the experimental deviations from the simulated values were less than 1.5%. This finding suggests that the device is a promising candidate to be used, for instance, for dosimetry purposes in the treatment of melanoma of the uveal tract (i.e., iris, choroid, or ciliary body) or pediatric central nervous system tumors [46], to name a few cases where ^{4}He ions are being exploited.

For mean deposited energies between 32.52 MeV/mm and 86.74 MeV/mm, the used assembly presented a non-linear response. Consequently, deviations from around 14% to 64% from the simulated values were observed. Such deviations were mainly attributed to the read-out chip's inability to record and process very high signals. Moreover, the next generation of Timepix, the Timepix3 detector, could be able to reduce the observed underestimations in the deposited energy.

With regard to the widths of the analyzed spectra, it was found that all measurements resulted in wider distributions in comparison to the expectations from Monte Carlo simulations. The associated deviations ranged from 1.1% to 306%, being ^{12}C and ^{16}O the ion beams in which measurements presented the biggest differences.

When compared with a fully depleted 300 μm thick silicon sensor, the sensor used in this work showed an improved accuracy in measuring energy loss when the shape of the spectra and the mean deposited energy are considered. For ^{4}He and ^{12}C beams with the highest amount of deposited energy the deviations from the simulated mean deposited energy were 9 and 4 times smaller, respectively. This resulted from an extended range of linearity of the detector response which was observed for the fully depleted 100 μm sensor with respect to the 300 μm fully depleted sensor.

Between a mean deposited energy of 18.196 MeV/mm and 55.43 MeV/mm, the measurements with a partially depleted 300 μm thick device exhibited smaller deviations than the 100 μm sensor.

All in all, the findings of this thesis demonstrate that the 100 μm thick Timepix detector is capable of measuring energy loss with improved accuracy than a 300 μm sensor concerning the mean deposited energy and the width of the deposited energy spectrum for a mean energy deposition of up to 9.428 MeV/mm. Good reproducibility with regard to the shape of the energy loss spectra was accomplished with the 100 μm Timepix detector, too. Lower relative deviations of up to 27 times for ^{4}He beams and up to 4 times for ^{12}C beams were reached with the 100 μm thick detector (compared with the 300 μm thick sensor). There is still room for improvement in the region of high energy deposits considering that the presence of detector artifacts can highly deteriorate the

measured spectra. However, low energy deposits were better detected and processed by the 300 μm sensor.

The outcome of this experimental research brings to evidence the reliable performance of the employed 100 μm silicon sensor for proton and helium ion energy deposition measurements. The observed enhanced accuracy in this kind of measurements can be exploited to assess characteristics and properties of a given media. Therefore, the Timepix assembly with a sensitive layer of 100 μm thick has great potential in ion beam radiography applications.

Bibliography

[1] World Health Organization [Internet]. Switzerland: World Health Organization; 2018. News. [unknown date] [cited 2018 Jun 6]; [about 3 screens]. Available from: http://www.who.int/news-room/fact-sheets/detail/cancer

[2] American Cancer Society [Internet]. USA GA: American Cancer Society; 2018. Cancer Information: Cancer Facts & Statistics: Global Cancer Facts & Figures. 2015 [cited 2018 Jun 6]; [about 64 screens]. Available from: https://www.cancer.org/content/dam/cancer-org/research/cancer-facts-and-statistics/global-cancer-facts-and-figures/global-cancer-facts-and-figures-3rd-edition.pdf

[3] World Health Organization [Internet]. Switzerland: World Health Organization; 2018. News/Fact sheets/Detail. 2018 Feb 1 [cited 2018 Jun 6]; [about 3 screens]. Available from: http://www.who.int/news-room/fact-sheets/detail/cancer

[4] Delaney G, Jacob S, Featherstone C and Barton M. The role of radiotherapy in cancer treatment: Estimating the optimal utilization from a review of evidence-based clinical guidelines. Cancer [Internet]. 2005 Sep 15 [cited 2018 Jun]; 104(6): 1129-1137. DOI: 10.1002/cncr.21324

[5] Kitagawa A, Fujita T, Muramatsu M, Biri S and Drentje AG. Review on heavy ion radiotherapy facilities and related ion sources. Rev. Sci. Instrum. [Internet]. 2010 Feb [cited 2018 Jun]; 81(2): 02B909. DOI: 10.1063/1.3268510

[6] Jakubek J. Semiconductor Pixel detectors and their applications in life sciences. JINST. 2009 [cited 2018 May]; 4(1): P03013.

[7] Avasthi DK and Mehta GK. Ion Matter Interaction. Swift Heavy Ions for Materials Engineering and Nanostructuring, Springer Series in Materials Science 145. India: Capital Publishing Company. 2011 [cited 2018 May]. Chapter 2.

[8] Tolstikhina I, Imai M, Winckler M and Shevelko V. Introduction. In: Drake GF editors. Basic Atomic Interactions of Accelerated Heavy Ions in Matter, Springer Series on

Atomic, Optic and Plasma Physics 98. Switzerland: Springer International Publishing AG. 2018 [cited 2018 May]. Chapter 1.

[9] Cox JD and Ang KK. Physical and Biologic Basis of Radiation Therapy. In: Cox JD and Ang KK, editors. Radiation Oncology: Rationale, Technique, Results. 9th ed. China: MOSBY Inc Elsevier. 2009 [cited 2018 Jun]. p. 3-49.

[10] Tavenier S. Interactions of particles in matter. Experimental Techniques in Nuclear and Particle Physics [Internet]. Germany: Springer International Publishing AG. 2010 [cited 2018 May]. Chapter 2. DOI: 10.1007/978-3-642-00829-0.

[11] L'Annuzata MF. Beta Radiation and Beta Decay. Radioactivity: Introduction and History, from the Quantum to Quarks [Internet]. Netherlands: Elsevier; 2016 [cited 2018 Jun]. Chapter 6.

[12] International Commission on Radiation Units and Measurements. Fundamental quantities and units for ionizing radiation. J ICRU [Internet]. 2011 Oct [cited 2018 Jun]; 11(1). DOI: 10.1093/jicru/ndr007

[13] Niemantsverdriet M, van Goethem MJ, Bron R, Hogewerf W, Brandenburg S, Langendijk JA, et al. High and Low LET Radiation Differentially Induce Normal Tissue Damage Signals. Int. J. Radiation Oncol. Biol. Phys. [Internet]. 2012 Jul 15 [cited 2018 May]; 83(4): 1291-1297. DOI: 10.1016/j.ijrobp.2011.09.057

[14] Podgorsak EB. Basic Radiation Physics. Radiation Oncology Physics: A Handbook for Teachers and Students [Internet]. Austria: IAEA. 2005 [cited 2018 Apr]; Chapter 1.

[15] National Institute of Standards and Technology [Internet]. USA: USA.gov; [date unknown]. Radiation Physics Division/Physical Reference Data Portal/Reference Data/ Radiation Dosimetry Data/Stopping-Power & Range Tables for Electrons, Protons, and Helium Ions/Appendix. 2017 Jul 28 [cited 2018 Jun12]; [about 1 screen]. Available from: https://physics.nist.gov/PhysRefData/Star/Text/appendix.html

[16] National Institute of Standards and Technology [Internet]. USA: USA.gov; [date unknown] [cited 2018 Jun11]; [about 2 screens]. Available from: https://physics.nist.gov

[17] Leroy C and Rancoita PG. Physics and Properties of Silicon Semiconductor. Silicon Solid State Devices and Radiation Detection [Internet]. Singapore: World Scientific Publishing Co. 2012 [cited 2018 Feb]. Chapter 2.

[18] Sze SM and Ng KK. Appendixes. Physics of Semiconductor Devices [Internet]. USA: John Wiley & Sons Inc.; 2007 [cited 2018 Feb]. p.790.

[19] Byun SH. Radioisotopes and Radiation Methodology I, II [Lecture notes on internet]. Ontario: McMaster University, Department of Physics and Astronomy & Radiation Sciences Graduate Program; 2017 [cited 2018 Feb]. Available from: https://www.science.mcmaster.ca/radgrad/images/6R06CourseResources/4RA3--4RB3-Lecture-Note-1_Radioactivity_Revised.pdf

[20] Silicon detectors. [The depletion zone] [Image on internet]. [Place unknown]: Krammer M, Hartmann F; 2011 [cited on 2018 Jun 15]. Available from: https://indico.cern.ch/event/124392/contributions/1339904/attachments/74582/106976/IntroSilicon.pdf

[21] All about circuits. [The p-n junction] [Image on Internet]. Panama: EETech Media, LLC; 2017 [cited on 2018 Jun 15]. Available form: https://www.allaboutcircuits.com/textbook/semiconductors/chpt-2/the-p-n-junction/

[22] UniversitätsKlinikum Heidelberg. Title [Image on Internet]. Germany: Universität Heidelberg; [date unlnown] [cited on 2018 Feb]. Available from: https://www.klinikum.uni-heidelberg.de

[23] CERN [Internet]. Switzerland: The medipix collaboration; 2015. The collaborations/Medipix. 2016 [cited on 2018 Jan 24]; [about 1 screen]. Available from: https://medipix.web.cern.ch

[24] Llopart X, Ballabriga R, Campbell M, Tlustos L and Wong W. Timepix, a 65k programmable pixel readout chip for arrival time, energy and/or photon counting measurements. Nucl. Inst. Meth. Phys. Res. A. 2007 Oct 21 [cited 2018 Jan]; 581(1-2): 485-494.

[25] ADVACAM. [Timepix detector] [Image on Internet]. Czech Republic: Advacam s.r.o. 2013 [cited on 2018 Jan]. Available from: http://www.widepix.cz/index.php?p=products

[26] CERN Medipix Group. [Ionizing radiation through Si sensor] [Image on internet]. Netherlands: Placket R. 2009 Sep 16 [cited on 2018 Jan]. Available from: https://slideplayer.com/slide/4380889/

[27] Leroy C and Rancoita PG. Charged Particle Detectors. Silicon Solid State Devices and Radiation Detection [Internet]. Singapore: World Scientific Publishing Co. 2012 [cited 2018 Jan]. Chapter 5.

[28] Bergmann B. Title [Image on Internet]. The ARDENT project and neutron detection with Timepix devices: Bergann B; 2012 Dec 20 [cited 2018 Mar]. Available from: https://slideplayer.com/slide/7352521/

[29] Bearden JA. X-Ray Wavelengths. Rev. Mod. Phys.1967 Jan 1 [cited 2018 Feb]; 39(1): 78-99.

[30] Jakubek J. Precise energy calibration of pixel detector working in time-over-threshold mode. Nucl. Inst. Methods Phys. Res. A. 2010 Jun 20 [cited 2018 Jan]; 633(1): S262-S266.

[31] Gehrke T, Burigo L, Arico G, Berke S, Jakubek J, Turecek D, et al. Energy deposition measurements of single 1H, 4He, and 12C ions of therapeutic energies in a silicon pixelated detector. JINST. 2017 Apr 21 [cited 2018 Jan]; 12(1): P04025.

[32] Battistoni G, Broggi F, Brugger M, Campanella M, Carboni M, Empl A, et al. Applications of FLUKA Monte Carlo code for nuclear and accelerator physics. Nucl. Instrum. Methods Phys. Res. B. 2011 Dec 15 [cited 2018 Feb]; 269 (24): 2850-2856.

[33] FLUKA. Combinatorial Geometry [Image on Internet]. Italy: Tucows Inc.; 2000 [cited 2018 Jan]. Available from: http://www.fluka.org/content/course/NEA/lectures/Geometry.pdf

[34] Tessonier T, Marcelos T, Mairani A, Brons S and Parodi K. Phase space generation for Proton and Carbon Ion Beams for External Users' Applications at the

Heidelberg Ion Therapy Center. Front. Oncol. [Internet]. 2016 Jan 11 [cited 2018 Feb]; 5(297): 1-15. DOI: 10.3389/fonc.2015.00297

[35] FLUKA [Internet]. Italy: Tucows Inc.; 2000. Documentation/Manuals/Online Manual/Description of FLUKA input options /BEAM. 2005 [cited on 2018 Jun 25]; [about 2 screens]. Available from: http://www.fluka.org/fluka.php?id=man_onl&sub=12

[36] FLUKA [Internet]. Italy: Tucows Inc.; 2000. Documentation/Manuals/pdf Manual/Description of FLUKA input options /PHYSICS. 2005 Oct 12 [cited on 2018 Jun 25]; [about 464 screens]. Available from: https://www.fluka.org/free_download/course/jlab2012/Lectures/03_BasicInput_0412.pdf

[37] Krejci F, Jakubek J, Kroupa M, Bruza P and Panek D. Pixel detector Timepix operated in pile-up mode for pulsed imaging with ultra-soft X-rays. JINST [Internet]. 2012 Dec 12 [cited 2018 Mar]; 7(12): C12013. DOI: 10.1088/1748-0221/7/12/C12013

[38] Hartmann B, Granja C, Jakubek J and Martisíková M. A novel Method for Fragmentation Studies in Particle Therapy: Principles of Ion Identification. IJPT [Internet]. 2017 May [cited 2018 Apr]; 3(4): 439-49. DOI: 10.14338/IJPT-15-00003.1

[39] Jakubek J. Semiconductor Pixel detectors and their application in life sciences. JINST [Internet]. 2009 Mar 17 [cited 2018 Mar]; 4(1): P03013. DOI: 10.1088/1748-0221/4/03/P03013

[40] CERN lectures [Internet]. Switzerland: Stefano Meroli; 2016 [cited on 2018 Apr 12]; [about 1 screen]. Available from: http://meroli.web.cern.ch/Lecture_landau_ionizing_particle.html

[41] Schardt D, Elsässer T and Schulz-Ertner D. Heavy-ion tumor therapy: Physical and Biological benefits. Rev. Mod. Phys. 2010 Feb 19 [cited 2018 Mar]; 82(1): 383-425.

[42] Groom DE and Klein SR. Passage of particles through matter. Eur. Phys. J. C. [Internet]. 2000 Mar [cited 2018 Mar]; 15(1-4): 163-173. DOI: 10.1007/BF02683419

[43] Granja C, Jakubek J, Köster U, Platkevic M, Pospisil S. Response of the pixel detector Timepix to heavy ions. Nucl. Instrum. Methods Phys. Res. A. 2011 May [cited 2018 Feb]. 633 (1): S198-S202.

[44] CERN [Internet]. Switzerland: The medipix collaboration; [date unknown]. The collaboration/Medipix3. 2014 [cited on 2018 May 31]. Available from: https://medipix.web.cern.ch/technology-chip/timepix3-chip

[45] De Gaspari M, Alozoy J, Ballabriga R, Campbell M, Fröjdh E, Idarraga J, et al. Design of the analog front-end for the Timepix3 and Smallpix hybrid pixel detectors in 130 nm CMOS technology. JINST [Internet]. 2014 [cited 2018 May]; 9 (1): C01037. DOI: 10.1088/1748-0221/9/01/C01037

“It only seems impossible until it's done”.
Nelson Mandela

Acknowledgements

John F. Kennedy said once: “We must find time to stop and thank the people who make a difference in our lives”. In this very little piece of paper I would like to somehow express how blessed I feel for having coincided in time and space with the people who made and keep making big difference in my life. Doing this Master has meant a lot to me from the very beginning: challenges, excitement, sacrifices, apprenticeships, fears to be face and much more. Many people have accompanied me through this process and there are no words to describe how grateful I feel for being surrounded by such beautiful persons and for receiving so much from them.

First of all I would like to thank the Mexican government and CONACyT for giving me the financial resources to make this dream possible. I will try my best to compensate my country by making improvements in the Medical Physics area and being a committed professional.

I am also very thankful with Beatriz Sánchez for accepting me in this program and with all the teachers at PUC for their work and teaching. To my first supervisor, Mària Martišikovà, I have a very honest feeling of estimation and admiration for being so enthusiastic and humble regardless her academic career and experience and for always having a friendly smile for me. I would like to thank you in the first place for accepting me to carry out this research in your group, for all the patience, guidance, support, the nice talks during the lunch at DKFZ casino and for sharing the Slovak culture. I really appreciate that you made me feel confident and comfortable in your group. Thank you very much also to my second supervisor, Paola Caprile, for her willingness, time, advice, words of support and understanding. My gratitude goes also to Marcel Schäfer: you were very important from the beginning of this project, thanks for all the advice and for being so nice with me every time, I really appreciate your help and your always honest willingness to talk.

One of the greatest gifts I received in this master program were the life-lasting friendships I made: To my dearest *chiquichamos,* Dany, Javi, Nathie, Francisco, José Luis and César from the beautiful Chile (and Venezuela), gracias inmensas por las risas y por todos los momentos compartidos, desde las temidas y estresantes interrogaciones hasta las divertidísimas salidas a comer. De cada uno me llevo atesorados recuerdos que me acompañarán por siempre. Espero nuestros caminos se vuelvan a cruzar en un futuro. Javi, muchísimas gracias por ser una persona tan sincera y transparente, por compartir tu destreza culinaria conmigo y por regalarme tu compañía y la de tu mami. A Dany y a Dieguito, maravillosos seres humanos y amigos, mil gracias por ser y estar. Agradezco la cariñosa acogida durante mi estancia en Chile y por haberme permitido

convivir con sus bellas familias, ¡me hicieron sentir como en casa! From across the pond I had the blessing of knowing very lovely people: my guys Tim, Marvin, Carlo and Renato who made of each day abroad, a better day just by being there. Tim, you definitely were a key part of my thesis, thank you very much for the invaluable support and for letting me get to know you better, you are a great person with beautiful feelings. I wish you all the best in your personal projects and with Lisa. Marvincito, I have no words to thank you for injecting freshness and your German good manners to my days, for trying your best to explain me your language and culture (even withouth success) and for your interest in learning Spanish. Carlo, grazie tante per i gesti italiani, per aver condiviso il tuo gusto per la cucina e per tutte gli insegnamenti della tua bellissima lingua e del tuo paese. Mi paisano Renato, ¡qué curioso que nos hayamos encontrado tan lejos! Muchas gracias por poner la mexicanidad que tanta falta hace cuando uno está lejos de casa y por tus bien intencionados y oportunos consejos, espero verte pronto.

Very special thanks to my family: my parents, my baby brother Marquito (*rayito de luna*) and my sister Zarit (*baby*), who always were there for me with words of love and encouragement, looking out for me despite the distance. I am aware of all the precious moments we lost because of being apart, but I am convinced that through this experience we have strengthened our family ties. Your love comforts me each day. Gracias con mayúsculas a mi mami (*din dins*) por darme la vida, por tu dulzura, por siempre apoyar mis sueños más locos e imposibles y por creer firmemente en mí. Desde el fondo de mi corazón digo y sostengo que eres mi ángel en la Tierra, mi más grande soporte y ejemplo de lucha. Tu esencia me acompaña y me cobija siempre. Todo lo que soy te lo debo a ti y al incondicional y desinteresado esfuerzo que has hecho por nuestra familia, en especial por mí, desde hace más de 27 años. Mis logros son tuyos, te los dedico con mucho amor y humildad esperando poder retribuir un poquito todo tu amor y sacrificios, ojalá te sientas orgullosa de tu *coquito*.

Last but not least, thanks to my love and partner of life and adventures, my *habibi* Alicito. Hemos pasado por tanto a través de los años y hoy, que concluimos este atrevido sueño de hacer la maestría en el extranjero, veo hacia atrás y no hay nada que quisiera cambiar. Hemos ido creciendo en lo académico y en lo personal, aprendiendo todos los días el uno del otro, completándonos, llenándonos de experiencias increíbles. Gracias infinitas por darme fuerza y valentía en esta travesía y por haber apoyado la idea de emprender este proyecto. Por estar conmigo a pesar de las circunstancias y muchas veces de mí, por toda tu honestidad, nobleza, ternura y ocurrencias, que me han dado impulso desde hace 8 años y me abren nuevos y bellos horizontes que no conocería si no fuera a tu lado. Me siento muy orgullosa de todo lo que has alcanzado pero sobretodo de verte feliz y satisfecho. Nos esperan muchas más aventuras y sueños por conquistar. Sé que a pesar de todas las posibles dificultades y adversidades lograremos salir adelante, como hasta ahora, en este maravilloso viaje que es la vida.